DRAFT VERSION APRIL 27, 2020
Typeset using LATEX **twocolumn** style in AASTeX63

arXiv:2004.11740v1 [astro-ph.HE] 24 Apr 2020

Exploiting orbital constraints from optical data to detect binary gamma-ray pulsars

L. NIEDER,[1, 2] B. ALLEN,[1, 3, 2] C. J. CLARK,[4] AND H. J. PLETSCH[1]

[1] *Max-Planck-Institut für Gravitationsphysik (Albert-Einstein-Institut), 30167 Hannover, Germany*
[2] *Leibniz Universität Hannover, 30167 Hannover, Germany*
[3] *Department of Physics, University of Wisconsin-Milwaukee, P.O. Box 413, Milwaukee, WI 53201, USA*
[4] *Jodrell Bank Centre for Astrophysics, Department of Physics and Astronomy, The University of Manchester, M13 9PL, UK*

(Received XXXX; Revised YYYY; Accepted ZZZZ; Published AAAA)

ABSTRACT

It is difficult to discover pulsars via their gamma-ray emission because current instruments typically detect fewer than one photon per million rotations. This creates a significant computing challenge for isolated pulsars, where the typical parameter search space spans wide ranges in four dimensions. It is even more demanding when the pulsar is in a binary system, where the orbital motion introduces several additional unknown parameters. Building on earlier work by Pletsch & Clark, we present optimal methods for such searches. These can also incorporate external constraints on the parameter space to be searched, for example from optical observations of a presumed binary companion. The solution has two parts. The first is the construction of optimal search grids in parameter space via a parameter-space metric, for initial semi-coherent searches and subsequent fully-coherent follow-ups. The second is a method to demodulate and detect the periodic pulsations. These methods have different sensitivity properties than traditional radio searches for binary pulsars, and might unveil new populations of pulsars.

Keywords: gamma rays: stars – methods: data analysis

1. INTRODUCTION

The Large Area Telescope (LAT; Atwood et al. 2009) on the *Fermi* satellite has helped to increase the known Galactic population of gamma-ray pulsars to more than 250 pulsars[1] (for a review see, e.g., Caraveo 2014). However, in the recent *Fermi* LAT Fourth Source Catalog (4FGL; Abdollahi et al. 2020) 1,525 out of 5,098 gamma-ray sources remain unassociated. Many of those are thought to be pulsars, perhaps in binary systems.

Gamma-ray pulsars may be detected in three ways. (a) A known (radio or X-ray) pulsar position and ephemeris guides a follow-up gamma-ray pulsation search within a nearby LAT source (e.g., Abdo et al. 2009a,b; Guillemot et al. 2012). (b) A similar gamma-ray pulsation search is done for a known pulsar, but *without* an obvious gamma-ray source being present (Smith et al. 2017). (c) A "blind" search hunts for gamma-ray pulsations around a LAT source where no pulsar has yet been identified.

Blind gamma-ray searches are the focus of this paper. Such searches have discovered more than 50 young pulsars (YPs) (e.g., Abdo et al. 2009c; Saz Parkinson et al. 2010; Clark et al. 2017), and three millisecond pulsars (MSPs) (Pletsch et al. 2012a; Clark et al. 2018). Many of these pulsars could not have been found via radio or X-ray emissions, which were not detected in extensive follow-up searches. Such systems are of particular interest because they constrain models of pulsar emission and beaming. Blind searches also have the potential to discover new populations of pulsar/neutron star objects.

So far, most blind gamma-ray searches have targeted isolated pulsars. The searches are a substantial computing effort, and have been carried out in campaigns or surveys that last several years. More recent surveys find new systems because the ongoing LAT operations provide additional data, which enables the detection of weaker pulsations (e.g., Clark et al. 2017). However, there is also a downside: the computing power required also increases quickly with longer observation time spans.

Corresponding author: L. Nieder
lars.nieder@aei.mpg.de

---

[1] https://tinyurl.com/fermipulsars

Until now, blind gamma-ray searches have only found one binary MSP, PSR J1311−3430. This is tantalizing because three quarters of the known MSPs in the Australia Telescope National Facility (ATNF) Pulsar Catalogue[2] (Manchester et al. 2005) are in binaries. So if search sensitivity were not limited by computing power, it might be possible to find many more. But even for isolated pulsars it is expensive to search for high ($> 100\,\mathrm{Hz}$) spin frequencies, and adding (at least three) additional orbital parameters makes it even more costly. By improving the techniques, the methods presented here are a first step towards finding more of these systems.

Much of our focus is on binary pulsars in so-called "spider" systems, in which the pulsar companion is being evaporated by an energetic pulsar wind. A typical example is the first "black widow" pulsar to be discovered, PSR B1957+20 (Fruchter et al. 1988). This was found in radio, where pulsations are eclipsed for a large fraction of the orbit, presumably by material ablated from the companion. Spider pulsars are categorized as black widows if the companion mass M_c is very low ($M_\mathrm{c} \ll 0.1\,M_\odot$) or as "redbacks" (another spider species) for larger companion masses ($M_\mathrm{c} \sim 0.15-0.4\,M_\odot$) (e.g., Roberts 2013).

For many of the known MSPs in spider systems, the companions are visible in the optical. The light originates from nuclear burning, and/or from pulsar wind heating up the companion. The orbital motion of the companion then leads to a detectable modulation of the orbital brightness. The source of this modulation is not well understood. It might be that the side of the companion facing the pulsar is hotter than the other side, and is more visible at the companion's superior conjunction. The companion might also be tidally elongated into an ellipsoid, whose projected cross section onto the line of sight varies over the orbit.

The new blind search methods presented here are well suited to gamma-ray pulsars in spider systems, with nearly circular orbits (eccentricity $e < 0.05$) and for which optical observations of the pulsar's companion provide information about the orbital motion, and thus constrain the gamma-ray pulsation search space.

For concreteness, we present the search designs for two promising gamma-ray sources: (a) 3FGL J1653.6–0158, a likely MSP in a circular binary (Romani et al. 2014; Kong et al. 2014), and (b) 3FGL J0523.3–2528, a probable MSP in a slightly eccentric binary (Strader et al. 2014). These are ranked among the most likely pulsar candidates (Saz Parkinson et al. 2016). We demonstrate the feasibility of a search using the computing resources of the distributed volunteer computing project *Einstein@Home* (Allen et al. 2013).

The paper is organized as follows. Section 2 reviews blind search methods for isolated gamma-ray pulsars and introduces the concepts required for such searches. Section 3 extends the methods to gamma-ray pulsars in circular orbit binaries and Section 4 further extends these to eccentric orbit binaries. In Section 5 our methods are compared with alternatives used in radio and gravitational-wave astronomy. Finally, in Section 6 we discuss the feasibility of future blind searches for binary gamma-ray pulsars and also consider some specific sources. This is followed by Appendices A, B, and C containing some technical details.

In this paper, c denotes the speed of light and G denotes Newton's gravitational constant.

2. BLIND SEARCHES FOR GAMMA-RAY PULSARS

Blind-search methods for isolated gamma-ray pulsars have been studied in detail by Pletsch & Clark (2014). Here, we summarize and extend their framework. The following Sections generalize the search methods to binary pulsars.

The search for gamma-ray pulsations begins with a list of N photons from a posited source, which we label with the index $j = 1, \dots, N$. The data available for these photons are their detector arrival time t_j, their direction of origin, and their energy, spanning an observation interval T_obs.

We are dealing with many sums and products in this paper. Sums and products over j, k, ℓ run from $1, \dots, N$ unless otherwise specified. Furthermore, we adopt the notation

$$\sum_{j \neq k} \equiv \sum_{j=1}^{N} \sum_{\substack{k=1 \\ j \neq k}}^{N} \tag{1}$$

for simplicity reasons.

Not all photons are equally significant. Photons at low energies are less well-localized than those at higher energies, and cannot be so readily attributed to a target source. Photons whose energy is more consistent with a distributed background are less likely to come from the pulsar. Photons originating from a nearby point source might contaminate the data set. For such reasons, searches may be improved by modeling the spatial and energy distribution of the sources. This assigns a weight $w_j \in [0, 1]$ to each photon, which is the only place where the energy and arrival direction of the photons enter our analysis. The weight w_j represents the probability that the j'th photon originated at the nominal pulsar (Bickel et al. 2008; Kerr 2011). These weights are used for noise suppression and to reduce computing cost by removing the lowest-weighted photons. In this paper, we assume that these weights have been determined in advance for each photon, so the only information available for the j'th photon is its arrival time t_j in the detector and the weight w_j.

The question that we need to answer is, are the arrival times of these photons random, or is there an underlying periodicity? To answer this question (in the statistical sense), we first need a model for the periodicity, which we assume is tied to the physical rotation of the pulsar.

---

[2] http://www.atnf.csiro.au/research/pulsar/psrcat

2.1. *Pulse profile and photon arrival probability*

For now, assume that "in isolation" the pulsar would have a linearly-changing angular velocity. Using Φ to denote the rotational phase in radians

$$\Phi(t_{\mathrm{psr}}, \boldsymbol{\lambda}) = 2\pi f (t_{\mathrm{psr}} - t_{\mathrm{ref}}) + \pi \dot{f} (t_{\mathrm{psr}} - t_{\mathrm{ref}})^2 , \tag{2}$$

where t_{psr} is the time that would be measured by a fictitious observer freely falling with the center of mass of the pulsar, and t_{ref} is a reference time. Note that detector time ticks at a different rate than t_{psr}, because the detector is moving around the Earth and Sun, and because the pulsar might be orbiting a binary companion, or accelerating towards the Galaxy. Also note that without loss of generality we have set the phase at the reference time to zero.

The parameters $\boldsymbol{\lambda}$ describe the pulsar. Here they are the spin frequency f and its first time derivative $\dot{f}$ at reference time t_{ref}. This second-order Taylor approximation holds for many pulsars and most MSPs, but for very young and "glitching" pulsars, additional higher order terms may be needed.

The flux of photons can be broken into three parts. The first does not come from the pulsar: it is a background which is uncorrelated with pulsar rotation. We call these unpulsed photons "background". The second part originates from the pulsar itself but is also uncorrelated with pulsar rotation. We call these "unpulsed source" photons. The last part is a periodically time-varying flux from the source, which we call "pulsed". We use p to denote the ratio of the number of pulsed photons to the total number of source photons (pulsed and unpulsed source).

The pulsed photon flux may be described with a periodic function $F_{\mathrm{S}}(\Phi)$ of the pulsar's phase around its rotational axis, $\Phi \in [0, 2\pi]$, and is time-stable for most pulsars. The normalized probability that a pulsed photon arrives in the phase interval $[\Phi, \Phi + \mathrm{d}\Phi]$ is $F_{\mathrm{S}}(\Phi)\,\mathrm{d}\Phi$. The function $F_{\mathrm{S}}(\Phi)$ has minimum value zero and encloses unit area in the interval $[0, 2\pi]$.

We can now give the probability density function for the rotation phase associated with a given photon. This differs from one photon to the next because photons with small weight w_j are more likely to have a phase-independent probability distribution. The probability that the j'th photon originates from a rotation phase interval $[\Phi_j, \Phi_j + \mathrm{d}\Phi_j]$ is $F_j(\Phi_j)\,\mathrm{d}\Phi_j$, where

$$F_j(\Phi_j) = \frac{1 - w_j}{2\pi} + w_j \left[\frac{1 - p}{2\pi} + p F_{\mathrm{S}}(\Phi_j) \right] . \tag{3}$$

The first term (with probability $1 - w_j$) describes the background photons, and the second and third terms (with probability w_j) the unpulsed and pulsed source photons respectively.

The probability distribution of pulsed photons may be expressed as the Fourier series

$$F_{\mathrm{S}}(\Phi) = \frac{1}{2\pi} + \frac{1}{2\pi} \sum_{n=1}^{\infty} \left(\gamma_n \mathrm{e}^{in\Phi} + \gamma_n^* \mathrm{e}^{-in\Phi} \right) . \tag{4}$$

The complex Fourier coefficients are

$$\gamma_n = \int_0^{2\pi} F_{\mathrm{S}}(\Phi) \mathrm{e}^{-in\Phi} \, \mathrm{d}\Phi . \tag{5}$$

Note that the Fourier coefficients γ_n are constrained because F_{S} has minimum value zero. Note also that for known gamma-ray pulsars $|\gamma_n|^2$ decreases quickly with increasing index n (Pletsch & Clark 2014). In many cases the first 5 harmonics are sufficient to describe the pulse profile.

In principle, to detect gamma-ray pulsations, we assume a rotational model $f, \dot{f}$ and then compute the rotational phase associated with each photon. "Binning" these phases (mod 2π) with weights w_j provides an estimate of $F(\Phi) = \sum_j w_j F_j(\Phi) / \sum_j w_j$, from which we can estimate $F_{\mathrm{S}}(\Phi)$ by shifting the minimum value to zero and re-scaling to unit area. If that function is compatible with zero (meaning: coefficients γ_n are small), then no pulsations were detected. Conversely, if the γ_n are large for some values of f and $\dot{f}$, we have found pulsations.

2.2. *Relationship of detector time t to t_{psr}*

The situation is slightly more complicated than described in the previous paragraph because computing t_{psr} for each photon from its time of arrival at the *Fermi* satellite also requires the pulsar's sky position (right ascension α and declination δ). The sky position allows for " barycentric corrections", e.g., to account for Doppler shifts due to the LAT's movement around the Solar System Barycenter (SSB). Thus the photon's emission time $t_{\mathrm{psr}}(t, \alpha, \delta)$ is a function of its arrival time t at the LAT and the putative pulsar's sky position. The pulsar's putative phase is a function of t and the four parameters $\boldsymbol{\lambda} = \{f, \dot{f}, \alpha, \delta\}$.

In blind searches the spin parameters are unknown. Although each photon is tagged with an arrival direction α, δ, these are not sufficiently precise to detect pulsations, so those location parameters must also be searched. Hence the parameter-space search volume Λ for isolated pulsars ($\boldsymbol{\lambda} \in \Lambda$) is 4-dimensional. In Sections 3 and 4, the higher-dimensional search spaces for binary pulsars in circular and elliptical orbits are discussed.

2.3. *Searching for pulsations*

For realistic searches the parameter space Λ is too large to search by the straightforward computational process described above. Instead Λ is explored with a multistage search based on several different test statistics (e.g., Meinshausen et al. 2009). This gives the greatest sensitivity at fixed computational cost (Pletsch & Clark 2014). The approach is hierarchical. In the first stage, a coarse grid covering the parameter space Λ is searched at low sensitivity using inexpensive test statistics. These are relatively insensitive to mismatch between tested parameters and pulsar parameters. In the following stages, smaller regions of Λ around the most promising candidates are searched at higher sensitivity. These use more expensive test statistics on finer, more closely spaced grids. Thus, a search is defined by a test statistic/grid hierarchy.

The spacing of the grids in parameter space is governed by the mismatch described above. For a given test statistic, we calculate a "metric", which is the fractional loss in the expected signal-to-noise ratio (S/N). The details of this are found later in this Section.

The search described in this paper has four stages, which employ detection statistics P_1, S_1, and H. Here we briefly describe the overall structure. The test statistics are defined and characterized later in this Section.

The first three stages search for significant power in the first harmonic $|\gamma_1|^2$. Each discards regions of parameter space which contain no signals; what remains is passed to the following stage. The first stage uses the "semi-coherent" test statistic S_1 with a low threshold. The second stage tests S_1 on a finer grid, with a higher threshold. The third stage uses the fully coherent test statistic P_1. This searches coherently for power $|\gamma_1|^2$ over the full observation span T_{obs} with much greater sensitivity and a finer grid than before.

The fourth stage employs the expensive H statistic, which combines $P_1, \ldots, P_5$. This coherently integrates over T_{obs} to identify power in the first five harmonics $|\gamma_1|^2, \ldots, |\gamma_5|^2$. By searching around the surviving candidate points in parameter space with a still finer grid, this completes the hierarchy.

2.4. *Coherent power test statistic P*

The basis for all of our test statistics is the coherent Fourier power, evaluated over different periods of time. For the n'th harmonic, and including all of the photons, this is

$$P_n(\boldsymbol{\lambda}) = \frac{1}{\kappa^2}\Big|\sum_j w_j \mathrm{e}^{-in\Phi(t_j,\boldsymbol{\lambda})}\Big|^2. \tag{6}$$

To simplify notation, from here on we use $\Phi(t_j,\boldsymbol{\lambda})$ to denote $\Phi(t_{\text{psr}}(t_j,\alpha,\delta),f,\dot{f})$, where t_j is the photon arrival time measured at the LAT. The normalization constant is

$$\kappa^2 = \frac{1}{2}\sum_j w_j^2 . \tag{7}$$

How does P_n behave in the absence of pulsations and in the presence of pulsations?

To answer this question, we compute expectation values as shown in Appendix A. The power P_n has an expected value (Eq. A5) and variance (in the absence of a pulsed signal, $p = 0$)

$$\mathrm{E}_p[P_n] = 2 + \kappa^{-2} p^2 |\gamma_n|^2 \sum_{j\neq k} w_j^2 w_k^2 \tag{8}$$

$$\mathrm{Var}_0[P_n] = \kappa^{-4} \sum_{j\neq k} w_j^2 w_k^2 . \tag{9}$$

The power P_n is a *detection statistic* because it is sensitive to a non-vanishing pulse profile. If γ_n is non-zero, then P_n should be larger than two. It becomes larger as the fraction p of pulsed to source photons increases (which we cannot control). It also becomes larger as the number of photons (or equivalently, the observation time) grows. But to understand what values of P_n correspond to statistically significant detections, we need to know about its statistical fluctuations, meaning the variance in P_n.

Note that the diagonal-free double sum in these expressions can be re-expressed as $(\sum_j w_j^2)^2 - \sum_j w_j^4$. Thus the variance can be written

$$\mathrm{Var}_0[P_n] = 4 - 4\frac{\sum_j w_j^4}{(\sum_j w_j^2)^2} . \tag{10}$$

If there are many photons from the source, and the weights are relatively uniformly distributed, then it follows that the numerator in Eq. 10 is $\mathcal{O}(N)$ and the denominator is $\mathcal{O}(N^2)$. Hence, the variance $\mathrm{Var}_0[P_n] \to 4 - \mathcal{O}(1/N)$ approaches 4. In this limit, and with the statistical assumptions of Appendix A, P_n has a non-central χ^2-distribution with two degrees of freedom (Pletsch & Clark 2014). The non-centrality parameter is the second term appearing in Eq. (8).

The expected S/N associated with P_n is

$$\begin{aligned}\theta^2_{P_n} = \frac{\mathrm{E}_p[P_n] - \mathrm{E}_0[P_n]}{\sqrt{\mathrm{Var}_0[P_n]}} &= p^2|\gamma_n|^2 \sqrt{\sum_{j\neq k} w_j^2 w_k^2} \\ &= p^2|\gamma_n|^2 \mu\, T_{\text{obs}} .\end{aligned} \tag{11}$$

In the many-photon limit the quantity $\mu \to \sum_j w_j^2 / T_{\text{obs}}$ is proportional to the mean weighted photon arrival rate.

2.4.1. *Loss of P from parameter mismatch*

In a real search, we compute detection statistics at a grid of discrete values of the signal parameters $\boldsymbol{\lambda}$. If there is a signal present, its actual (true) parameters might be close to one of these discrete values, but will not match it exactly. There will always be *some* offset between the tested parameters and the true parameters. Here we quantify how much signal-to-noise is expected to be lost because of this mismatch.

Assume that the tested parameters $\boldsymbol{\lambda}$ are close to the true pulsar parameters $\boldsymbol{\lambda}_{\rm psr}$, and introduce the notation

$$\mathrm{d}\lambda^a = \lambda^a - \lambda^a_{\rm psr} \tag{12}$$

for the small parameter offsets. Here and elsewhere in the paper we index the parameter space dimension with lower-case Latin letters "a" and "b". These offsets change the pulsar rotation phase by

$$\Delta\Phi(t) = \Phi(t, \boldsymbol{\lambda}) - \Phi(t, \boldsymbol{\lambda}_{\rm psr}) \approx \partial_a \Phi \, \mathrm{d}\lambda^a \,, \tag{13}$$

where the notation

$$\partial_a \Phi = \left. \frac{\partial \Phi}{\partial \lambda^a} \right|_{\boldsymbol{\lambda} = \boldsymbol{\lambda}_{\rm psr}} \tag{14}$$

is introduced and we neglect higher powers in $\mathrm{d}\lambda$. We also adopt the *Einstein summation convention* that repeated parameter space indices are summed over all the dimensions of the parameter space.

We now compute the fractional loss in expected S/N associated with this parameter mismatch. For the offset parameters the coherent power is

$$P_n(\boldsymbol{\lambda}) = 2 + \kappa^{-2} \sum_{j \neq k} w_j w_k \mathrm{e}^{in(\Phi_j - \Phi_k)} \mathrm{e}^{in(\Delta\Phi_j - \Delta\Phi_k)} \,, \tag{15}$$

where $\Phi_j = \Phi(t_j, \boldsymbol{\lambda}_{\rm psr})$ and $\Delta\Phi_j = \Delta\Phi(t_j)$. Following Appendix A, the expectation value of this is

$$\mathrm{E}_p[P_n(\boldsymbol{\lambda})] = 2 + \kappa^{-2} p^2 |\gamma_n|^2 \sum_{j \neq k} w_j^2 w_k^2 \mathrm{e}^{in(\Delta\Phi_j - \Delta\Phi_k)} \,. \tag{16}$$

It follows that for the mismatched signal the expected S/N is

$$\theta^2_{P_n(\boldsymbol{\lambda})} = p^2 |\gamma_n|^2 \left[\sum_{j \neq k} w_j^2 w_k^2 \right]^{-1/2} \sum_{j \neq k} w_j^2 w_k^2 \mathrm{e}^{in\left(\Delta\Phi_j - \Delta\Phi_k\right)} \,. \tag{17}$$

The fractional loss in S/N (often called the "mismatch") is

$$\begin{aligned} m(\boldsymbol{\lambda}, \boldsymbol{\lambda}_{\rm psr}) &= \frac{\theta^2_{P_n}(\boldsymbol{\lambda}_{\rm psr}) - \theta^2_{P_n}(\boldsymbol{\lambda})}{\theta^2_{P_n}(\boldsymbol{\lambda}_{\rm psr})} \\ &= \sum_{j \neq k} w_j^2 w_k^2 \left[1 - \mathrm{e}^{in(\Delta\Phi_j - \Delta\Phi_k)} \right] \Big/ \sum_{j \neq k} w_j^2 w_k^2 \\ &= \left[\left(\sum_j w_j^2 \right)^2 - \left| \sum_j w_j^2 \mathrm{e}^{in\Delta\Phi_j} \right|^2 \right] \Bigg/ \left[\left(\sum_j w_j^2 \right)^2 - \sum_j w_j^4 \right] \,. \end{aligned} \tag{18}$$

We need the mismatch to help set the spacings of the parameter space search grids, but for that purpose, approximations suffice.

Assume there are many photons, and the weights are uniformly distributed in time (or at least slowly varying in a way that is not correlated with the pulsar rotation phase). The sums over the weights may then be replaced with simple integrals over time, giving

$$m(\boldsymbol{\lambda}, \boldsymbol{\lambda}_{\rm psr}) \approx 1 - \left| {}_{T_{\rm obs}}\!\left\langle \mathrm{e}^{-in\Delta\Phi(t)} \right\rangle\!(t_0) \right|^2 \,. \tag{19}$$

Here we introduce "angle bracket" notation for an average over a time interval of length T centered around an arbitrary time t_0. This takes an input function $Q(t')$ and outputs a new function of time t defined by

$${}_T\langle Q(t') \rangle(t) \equiv \frac{1}{T} \int_{t-T/2}^{t+T/2} Q(t') \, \mathrm{d}t' \,, \tag{20}$$

which is the average of Q around the time t.

2.4.2. *Parameter space metric g_{ab}*

Since the sensitivity of these searches is limited by available computing power, we need to construct a grid that covers the relevant parameter space with the smallest number of grid points. This means that the parameters $\boldsymbol{\lambda}_{\rm psr}$ of any possible pulsar should be close enough to a grid point that we do not lose too much S/N from the mismatch, but the grid should have as few points as possible.

The distance metric on the search space is a useful tool for such constructions (Balasubramanian et al. 1996; Owen 1996). It provides an analytical approximation to the mismatch. For example, the coherent mismatch in Equation (19) can be approximated by the "coherent metric" g_{ab}

$$m(\boldsymbol{\lambda}, \boldsymbol{\lambda}_{\rm psr}) = n^2 g_{ab}(\boldsymbol{\lambda}) \, \mathrm{d}\lambda^a \, \mathrm{d}\lambda^b + \mathcal{O}(\mathrm{d}\lambda^3) \tag{21}$$

for small coordinate offsets $\mathrm{d}\lambda^a$ from the true pulsar parameters.

Expanding the exponential that appears in Eq. (19) to first order, one finds

$$g_{ab} = {}_{T_{\rm obs}}\langle \partial_a \Phi \partial_b \Phi \rangle(t_0) - {}_{T_{\rm obs}}\langle \partial_a \Phi \rangle(t_0) \, {}_{T_{\rm obs}}\langle \partial_b \Phi \rangle(t_0) \,. \tag{22}$$

To evaluate the metrics, we need to account for the way in which the detected pulsar rotation phase depends upon the different pulsar parameters.

2.4.3. *Evaluation of g_{ab} for isolated pulsars*

As seen by an observer freely falling at the center of mass of the pulsar, the rotation phase just depends upon the intrinsic frequency f and its derivative $\dot{f}$ as given in Eq. 2. But as explained in Sec. 2.2, these must be converted to detector time.

For computing the metric, we do not need a conversion that is accurate to microseconds, but only one that takes into account the largest shifts between detector and pulsar time, of order $\approx 500\,\mathrm{s}$, arising from the motion of the Earth around the Sun (Pletsch & Clark 2014). We denote the orbital angular frequency $\Omega_\mathrm{E} = 2\pi/\mathrm{yr}$, the orbital light-crossing time by $r_\mathrm{E} = 1\,\mathrm{AU}/c$, and the obliquity of the ecliptic by $\epsilon = 23.4°$.

If we choose a coordinate axis z along the line of sight to the pulsar, the the projected motion is

$$r_{z,\mathrm{sky}}(t) = r_\mathrm{E}\left[n_\mathrm{x}\cos(\Omega_\mathrm{E}t+\varphi_\mathrm{ref})+n_\mathrm{y}\sin(\Omega_\mathrm{E}t+\varphi_\mathrm{ref})\right], \tag{23}$$

where

$$n_\mathrm{x} = \cos\alpha\cos\delta\,, \tag{24}$$

$$n_\mathrm{y} = \cos\epsilon\sin\alpha\cos\delta+\sin\epsilon\sin\delta\,, \tag{25}$$

and the sky location is given by the right ascension α, and the declination δ. The (arbitrary) choice for the origin of the time coordinate determines the constant φ_ref, which is the Earth's orbital phase at that moment.

Note that this simplified version of the Rømer delay does not account for the motion of the *Fermi* satellite around the Earth. It is not accurate enough to use in a search for pulsations, and is only used in the metric calculation.

For the purpose of computing the metric we can model the detected pulsar rotation phase as the sum of (2) and the additional phase cycles introduced by the Rømer delay (23):

$$\begin{aligned}\Phi(t,\boldsymbol{\lambda}) = {} & 2\pi f(t-t_\mathrm{ref})+\pi\dot{f}(t-t_\mathrm{ref})^2 \\ & +2\pi f r_\mathrm{E}\left[n_\mathrm{x}\cos(\Omega_\mathrm{E}t+\varphi_\mathrm{ref})+n_\mathrm{y}\sin(\Omega_\mathrm{E}t+\varphi_\mathrm{ref})\right].\end{aligned} \tag{26}$$

Here, the search parameters are $\boldsymbol{\lambda} = \{f,\dot{f},n_x,n_y\}$, and the terms correcting the arrival times t have been neglected for the $\dot{f}$ summand.

The metric for the coherent power P_1 follows from Eq. (22). The formulae are complicated but if we keep only the most significant terms then they simplify. To determine these, consider the relative size of the different quantities:

$$\begin{aligned} T_\mathrm{obs} &\approx 10\ \mathrm{yr} \approx 3\times10^{8}\,\mathrm{s}\,, \\ |t_0-t_\mathrm{ref}| &\lesssim T_\mathrm{obs}\,, \\ \Omega_\mathrm{E} &\approx 2\pi/\mathrm{yr} \approx 2\times10^{-7}\,\mathrm{s}^{-1}\,, \\ r_\mathrm{E} &\approx 5\times10^{2}\,\mathrm{s}\,, \\ f &\approx (100-700)\,\mathrm{s}^{-1}\,, \\ \dot{f} &\approx (10^{-16}-10^{-14})\,\mathrm{s}^{-2}\,. \end{aligned} \tag{27}$$

Most MSPs have parameters f and $\dot{f}$ in the given range. With these in mind, one finds diagonal metric components

$$\begin{aligned} g_{ff} &= \frac{1}{3}\pi^2T_\mathrm{obs}^2\left[1+\mathcal{O}(r_\mathrm{E}/T_\mathrm{obs})\right], \\ g_{\dot{f}\dot{f}} &= \frac{1}{180}\pi^2T_\mathrm{obs}^4\left[1+60\frac{(t_0-t_\mathrm{ref})^2}{T_\mathrm{obs}^2}\right], \\ g_{n_xn_x} &= 2\pi^2f^2r_\mathrm{E}^2\left[1+\mathcal{O}(1/\Omega_\mathrm{E}T_\mathrm{obs})\right], \\ g_{n_yn_y} &= 2\pi^2f^2r_\mathrm{E}^2\left[1+\mathcal{O}(1/\Omega_\mathrm{E}T_\mathrm{obs})\right]. \end{aligned} \tag{28}$$

Most of the off-diagonal metric components are negligible.

Determining if off-diagonal metric components are significant requires some care because they need to be compared to the corresponding diagonal components. This arises here, and in several other places in the paper. Here, we show in detail how this significance is determined. The same reasoning is used for the other cases that arise later, but is not elaborated.

Since the fundamental quantity of interest is the mismatch m, for fixed a and b (no Einstein summation convention), consider $m = g_{aa}(\mathrm{d}\lambda^a)^2+g_{bb}(\mathrm{d}\lambda^b)^2+2g_{ab}\,\mathrm{d}\lambda^a\,\mathrm{d}\lambda^b$. Re-scale the coordinates $\{\lambda^a,\lambda^b\}$ to new coordinates $\{\lambda^{a'} = u\lambda^a, \lambda^{b'} = w\lambda^b\}$ such that the two diagonal components of the metric in the new coordinates are both unity. (Here, u and w denote the re-scaling factors.) This implies that $g_{aa}(\partial\lambda^a/\partial\lambda^{a'})^2 = g_{aa}u^{-2} = 1$ and $g_{bb}(\partial\lambda^b/\partial\lambda b')^2 = g_{bb}w^{-2} = 1$. Then all off-diagonal metric components are of $\mathcal{O}(1/\Omega_\mathrm{E}T_\mathrm{obs})$, apart from

$$g_{f\dot{f}} = \frac{1}{3}\pi^2T_\mathrm{obs}^3\left[\frac{(t_0-t_\mathrm{ref})}{T_\mathrm{obs}}+\mathcal{O}(r_\mathrm{E}/T_\mathrm{obs})\right]. \tag{29}$$

Note that all the off-diagonal terms may be neglected in the case that the integration time $T_\mathrm{obs} \gg 1\,\mathrm{yr}$ and the reference time $t_\mathrm{ref} = t_0$.

For this case the diagonal "coherent metric" terms reduce to

$$\begin{aligned} g_{ff} &= \frac{1}{3}\pi^2T_\mathrm{obs}^2\,, \\ g_{\dot{f}\dot{f}} &= \frac{1}{180}\pi^2T_\mathrm{obs}^4\,, \\ g_{n_xn_x} &= 2\pi^2f^2r_\mathrm{E}^2\,, \\ g_{n_yn_y} &= 2\pi^2f^2r_\mathrm{E}^2\,. \end{aligned} \tag{30}$$

2.5. *Semicoherent power test statistic S*

The coherent power P_n in (6) provides a good statistical basis to find pulsations (meaning γ_n nonzero) but is inefficient to compute. So the first two stages of our searches use the "semi-coherent" Fourier power S_n. Its definition is similar to P_n except that photons are only combined if their arrival-time difference is smaller than a coherence time, $T_\mathrm{coh} \ll T_\mathrm{obs}$. This makes it less expensive to compute (but also less sensitive). The coherence time in a typical search in the first stage is $T_\mathrm{coh} = 2^{21}\,\mathrm{s} \approx 24\,\mathrm{d}$, in the second stage is $T_\mathrm{coh} = 2^{22}\,\mathrm{s} \approx 48\,\mathrm{d}$, and the observation span T_obs (i.e. the operation time of the LAT) is more than 10 years.

For convenience the statistic S_n differs from P_n in one other way: we omit the diagonal $j = k$ terms in the sum. This ensures that in the no-signal ($p = 0$) case the expected value of S_n vanishes, with

$$S_n(\boldsymbol{\lambda}) = \frac{1}{\bar{\mathcal{K}}}\sum_{j\neq k}w_jw_k\mathrm{e}^{-in[\Phi(t_j,\boldsymbol{\lambda})-\Phi(t_k,\boldsymbol{\lambda})]}\hat{W}_{T_\mathrm{coh}}(\tau_{jk})\,. \tag{31}$$

The rectangular window function restricts the sum to photons in which the arrival time difference $\tau_{jk} = t_j - t_k$ (or "lag") is not larger than $T_{\rm coh}$:

$$\hat{W}_{T_{\rm coh}}(\tau) = \begin{cases} 1 & \text{for } |\tau| \le T_{\rm coh}/2\,, \\ 0 & \text{otherwise}\,. \end{cases} \tag{32}$$

The semi-coherent normalization constant is chosen to be

$$\bar{\kappa} = \sqrt{\sum_{j \neq k} w_j^2 w_k^2 \hat{W}^2_{T_{\rm coh}}(\tau_{jk})}\,, \tag{33}$$

which ensures that in the no-signal ($p = 0$) case S_n has unit variance (Clark et al. 2017).

To characterize this detection statistic, we calculate the expectation value and variance with the calculational framework of Appendix A, obtaining:

$$\mathrm{E}_p[S_n] = \frac{1}{\bar{\kappa}} p^2 |\gamma_n|^2 \sum_{j \neq k} w_j^2 w_k^2 \hat{W}_{T_{\rm coh}}(\tau_{jk})\,, \tag{34}$$

$$\mathrm{Var}_0[S_n] = 1\,. \tag{35}$$

The expectation value is the same as the second term of P_n in Eq. (8), except that the sum is restricted to the lag window. In fact, the formulae above hold for any choice of window function.

The S/N for the semi-coherent Fourier power S_n is simplified by assuming a rectangular window function (which equals its square). This gives

$$\begin{aligned} \theta^2_{S_n} &= \frac{\mathrm{E}_p[S_n] - \mathrm{E}_0[S_n]}{\sqrt{\mathrm{Var}_0[S_n]}} = p^2 |\gamma_n|^2 \sqrt{\sum_{j \neq k} w_j^2 w_k^2 \hat{W}_{T_{\rm coh}}(\tau_{jk})} \\ &= p^2 |\gamma_n|^2 \mu \sqrt{T_{\rm coh} T_{\rm obs}}\,. \end{aligned} \tag{36}$$

The second line adopts the definition of μ given after Eq. (11) and makes the same assumptions of steady photon flux and large photon number.

In practice, how large are these detection statistics? A typical gamma-ray pulsar might have a pulsed flux for which $|\gamma_1|^2 \approx 0.2$ and a 70%-fraction of pulsed photons for which $p^2 \approx 0.5$. The weighted flux of source photons detected might be $\sum_j w_j^2 \approx 500$ over $T_{\rm obs} = 10\,\mathrm{yr}$, implying a rate $\mu \approx 50/\mathrm{yr}$. With $T_{\rm coh} = 24\,\mathrm{d}$, this leads to coherent and incoherent S/Ns of order $\theta^2_{P_1} \approx 50$ and $\theta^2_{S_1} \approx 4$, significant at the 50σ and 4σ levels respectively.

2.5.1. *Loss of S from parameter mismatch*

We now turn to the metric for the semi-coherent statistic. To compute the mismatch for the semi-coherent detection statistic S_n, with the same assumptions as above, we can replace the sums with integrals, obtaining

$$\begin{aligned} \bar{m}(\boldsymbol{\lambda}, \boldsymbol{\lambda}_{\rm psr}) &= 1 - \frac{\theta^2_{S_n}(\boldsymbol{\lambda})}{\theta^2_{S_n}(\boldsymbol{\lambda}_{\rm psr})} \\ &= 1 - {}_{T_{\rm obs}}\!\Big\langle \mathrm{e}^{-in\Delta\Phi(t')}\; {}_{T_{\rm coh}}\!\Big\langle \mathrm{e}^{in\Delta\Phi(t'')} \Big\rangle(t') \Big\rangle(t_0)\,. \end{aligned} \tag{37}$$

Note that the inner integral in the second line can include times outside the observation span $t'' \in [t_0 - T_{\rm obs}/2, t_0 + T_{\rm obs}/2]$, going down to $t'' = t_0 - T_{\rm obs}/2 - T_{\rm coh}/2$ or up to $t'' = t_0 + T_{\rm obs}/2 + T_{\rm coh}/2$. In such cases the integrand should be set to zero, and normalized so that $\langle 1 \rangle = 1$.

2.5.2. *Parameter space metric $\bar{g}_{ab}$*

We now evaluate these mismatches to lowest order, obtaining a *distance metric* on the parameter space. We evaluate the integrals in Eq. (37) naively, without setting the integrands to zero outside of the "valid data range". This gives rise to terms (complex or linear in $\mathrm{d}\lambda^a$) which are not present in the exact expression. We assume that $T_{\rm coh} \ll T_{\rm obs}$ (typically $T_{\rm coh} = 24\,\mathrm{d}$ and $T_{\rm obs} > 10\,\mathrm{yr}$). In that case, these terms are small, and we discard them.

The partial derivatives with respect to $\lambda^a \in \{f, \dot{f}, n_x, n_y\}$, under the assumption that $T_{\rm coh} \ll 1\,\mathrm{yr} \ll T_{\rm obs}$, can be approximated as

$$\partial_a \Phi \approx {}_{T_{\rm coh}}\langle \partial_a \Phi \rangle(t)\,, \tag{38a}$$

$$\partial_a \partial_b \Phi \approx {}_{T_{\rm coh}}\langle \partial_a \partial_b \Phi \rangle(t)\,, \tag{38b}$$

as Pletsch & Clark (2014) did. (Here and in what follows, for readability, the time dependence of phase derivatives such as $\partial_a \Phi$ is not shown explicitly.)

With these assumptions the semi-coherent mismatch Eq. (37) can be approximated by the semi-coherent metric

$$\bar{m}(\boldsymbol{\lambda}, \boldsymbol{\lambda}_{\rm psr}) \approx n^2 \bar{g}_{ab}\, \mathrm{d}\lambda^a\, \mathrm{d}\lambda^b + \mathcal{O}(\mathrm{d}\lambda^3)\,, \tag{39}$$

where $\mathrm{d}\lambda^a = \lambda^a - \lambda^a_{\rm psr}$ as earlier. Note that Eq. (39) has the same form as the coherent mismatch in Eq. (21).

The metric components are

$$\begin{aligned} \bar{g}_{ab} &= {}_{T_{\rm obs}}\!\Big\langle {}_{T_{\rm coh}}\langle \partial_a \Phi \partial_b \Phi \rangle(t') - {}_{T_{\rm coh}}\langle \partial_a \Phi \rangle(t')\, {}_{T_{\rm coh}}\langle \partial_b \Phi \rangle(t') \Big\rangle(t_0)\,, \\ &= \frac{1}{2}\, {}_{T_{\rm obs}}\!\Big\langle \tilde{g}_{ab}(t') \Big\rangle(t_0)\,, \end{aligned} \tag{40}$$

where we have introduced

$$\tilde{g}_{ab}(t') = {}_{T_{\rm coh}}\langle \partial_a \Phi \partial_b \Phi \rangle(t') - {}_{T_{\rm coh}}\langle \partial_a \Phi \rangle(t')\, {}_{T_{\rm coh}}\langle \partial_b \Phi \rangle(t')\,, \tag{41}$$

which is exactly the coherent metric given in Eq. (22), but with $T_{\rm obs}$ replaced by $T_{\rm coh} \ll 1\,\mathrm{yr}$ and t_0 replaced by t'. Thus, terms of $\mathcal{O}(1/\Omega_{\rm E} T_{\rm coh})$, similar to those appearing in Eq. (28), cannot be neglected.

2.5.3. *Evaluation of $\bar{g}_{ab}$ for isolated pulsars*

The non-vanishing semi-coherent metric components are:

$$\begin{aligned}
\bar{g}_{ff} =& \frac{1}{6}\pi^2 T_{\mathrm{coh}}^2 \left[1+\mathcal{O}(r_{\mathrm{E}}/T_{\mathrm{obs}})\right] , \\
\bar{g}_{f\dot{f}} =& \frac{1}{6}\pi^2 T_{\mathrm{coh}}^2 T_{\mathrm{obs}} \left[\frac{(t_0-t_{\mathrm{ref}})}{T_{\mathrm{obs}}} + \mathcal{O}(r_{\mathrm{E}}/T_{\mathrm{obs}})\right] , \\
\bar{g}_{\dot{f}\dot{f}} =& \frac{1}{72}\pi^2 T_{\mathrm{coh}}^2 T_{\mathrm{obs}}^2 \left(1+12\frac{(t_0-t_{\mathrm{ref}})^2}{T_{\mathrm{obs}}^2} + \frac{T_{\mathrm{coh}}^2}{5T_{\mathrm{obs}}^2}\right) , \qquad (42) \\
\bar{g}_{n_x n_x} =& \pi^2 f^2 r_{\mathrm{E}}^2 \left[1-\frac{4}{\Omega_{\mathrm{E}}^2 T_{\mathrm{coh}}^2}\sin^2\!\left(\frac{\Omega_{\mathrm{E}} T_{\mathrm{coh}}}{2}\right) + \mathcal{O}(1/\Omega_{\mathrm{E}} T_{\mathrm{obs}})\right] , \\
\bar{g}_{n_y n_y} =& \pi^2 f^2 r_{\mathrm{E}}^2 \left[1-\frac{4}{\Omega_{\mathrm{E}}^2 T_{\mathrm{coh}}^2}\sin^2\!\left(\frac{\Omega_{\mathrm{E}} T_{\mathrm{coh}}}{2}\right) + \mathcal{O}(1/\Omega_{\mathrm{E}} T_{\mathrm{obs}})\right] .
\end{aligned}$$

The semi-coherent metric $\bar{g}$ is diagonal for $t_0 = t_{\mathrm{ref}}$, as was the case for the coherent metric g in Eq. (30). Note that $g_{n_x n_x}$ and $g_{n_y n_y}$ are not equal because the neglected terms of $\mathcal{O}(1/\Omega_{\mathrm{E}} T_{\mathrm{obs}})$ have opposite signs.

The metric component $\bar{g}_{f\dot{f}}$ differs from that given by Pletsch & Clark (2014), but our results are identical in the limit of a large number of photons N homogeneously distributed over the observation span. This is the case, since we assumed it in deriving Eqs. (19) and (37).

Comparison of Eqs. (28) and (42) illustrates the benefits of the multistage search process described in Section 2.3. For grids with the same mismatch $m = \bar{m}$, the ratio between the density of the coherent grid and the semi-coherent grid would be

$$\frac{\text{coherent grid density}}{\text{semi-coherent grid density}} = \sqrt{\frac{\det g}{\det \bar{g}}} = \frac{48 T_{\mathrm{obs}}^2}{\sqrt{5}\,\Omega_{\mathrm{E}}^2 T_{\mathrm{coh}}^4} . \qquad (43)$$

For the timescales T_{coh} and T_{obs} given above, the ratio $\sim 10^6$. This is why the semi-coherent search stage is beneficial.

2.6. *Multiple harmonic test statistic H*

In the last and most sensitive stage of the multistage search, we adopt the widely used statistic

$$H(\boldsymbol{\lambda}) = \max_{1\leq M\leq M_{\mathrm{max}}} \left(4-4M+\sum_{n=1}^{M} P_n(\boldsymbol{\lambda})\right) , \qquad (44)$$

which incoherently sums the coherent power from up to the first M_{max} harmonics in the pulse profile. The H statistic provides a sensitive test for unknown (generic) pulse profiles. The original simulations by de Jager et al. (1989) recommended $M_{\mathrm{max}} = 20$, and to assess the false-alarm probability, carried out a numerical study of the distribution of H in pure noise.

Later results by Kerr (2011) show that the single-trial probability ρ of exceeding a value $H_{\mathrm{threshold}}$ in pure noise is well modeled by $\rho \approx \exp(-0.398\,H_{\mathrm{threshold}})$ if the number of harmonics M_{max} is very large. Obviously, if M_{max} is reduced, then the single-trial probabilities are smaller than this, so $\exp(-0.4\,H_{\mathrm{threshold}})$ is a reliable upper bound.

To avoid over-fitting, we generally use smaller limits $M_{\mathrm{max}} = 3, 4,$ or 5 on the number of harmonics. Typical blind-search gamma-ray pulsar detections have H values in the hundreds, corresponding to single-trial ρ values which must lie below 10^{-30}.

Normally, the last search stage is not computationally limited. So we use a grid fine enough to secure power in the higher harmonics, while over-covering the search space for power in the lower harmonics. In practice, the grid is built using the coherent metric presented in Section 2.4.2 with $n = M_{\mathrm{max}}$.

2.7. *Searches for isolated pulsars*

Blind searches for isolated pulsars within gamma-ray data recorded by the LAT have been very successful (see, e.g., Clark et al. 2017). The key ingredients are the utilization of the powerful volunteer distributed computing system *Einstein@Home* (Allen et al. 2013) and searches which use these computing resources as efficiently as possible.

Most of the tools for constructing efficient searches have been presented in the earlier Sections. To discard unpromising regions in parameter space, the multistage approach is used as described in Section 2.3. For the first and computationally most crucial search stage, efficient grids covering the parameters $\dot{f}$, n_x, n_y are built based on the distance metric, and f is searched using fast Fourier transform (FFT) algorithms (Frigo & Johnson 2005). In later search stages, f is also gridded with the metric but it is not efficient to use FFTs on the small ranges in f around the few most significant candidates from the semi-coherent search stage.

3. SEARCH METHOD: CIRCULAR BINARY ORBITS

The main problem in blind searches for pulsars is that the phase model from equation (2) depends on the (photon emission) time at the pulsar, while a gamma-ray detector records the time of arrival at the telescope. For binary pulsars the largest corrections to shift between these two times arise from the line-of-sight motion of the *Fermi* satellite around Earth and Sun $r_{z,\mathrm{sky}}(t)$ and of the pulsar around its companion $r_{z,\mathrm{cir}}(t_{\mathrm{psr}})$.

The line-of-sight motion of a binary pulsar in a circular orbit can be described via 3 parameters, which are usually taken to be: the orbital frequency Ω_{orb}; the projected semi-major axis x in seconds; and the epoch of ascending node T_{asc}. With these, the two times are related by

$$t_{\mathrm{psr}} + r_{z,\mathrm{cir}}(t_{\mathrm{psr}}) = t + r_{z,\mathrm{sky}}(t) , \qquad (45)$$

where the corrections, also called Rømer delays, are expressed in seconds.

The simplest expression of the pulsar's orbital line-of-sight motion $r_{z,\mathrm{cir}}$ depends on the time measured at the pulsar t_{psr}. In many cases, this time may be replaced with the detector time because

$$r_{z,\mathrm{cir}}(t_{\mathrm{psr}}) = r_{z,\mathrm{cir}}(t)\,[1+\mathcal{O}\,(x\Omega_{\mathrm{orb}})]\,, \tag{46}$$

and the quantity $x\Omega_{\mathrm{orb}} \ll 1$. In such cases

$$t_{\mathrm{psr}} \approx t + r_{z,\mathrm{sky}}(t) - r_{z,\mathrm{cir}}(t)\,. \tag{47}$$

This holds for most black widow and some redback systems with projected semimajor axes in the order of a few light seconds (see, e.g., ATNF Pulsar Catalogue[3] by Manchester et al. 2005). In all cases, it is accurate enough to compute the metric, and in many cases accurate enough for maintaining phase coherence in a search.

The Rømer delay can be expressed in terms of the three orbital parameters as

$$r_{z,\mathrm{cir}}(t) = x\sin[\Omega_{\mathrm{orb}}(t-T_{\mathrm{asc}})]\,. \tag{48}$$

Here the orbital frequency Ω_{orb} is connected to the orbital period P_{orb} via $P_{\mathrm{orb}} = 2\pi/\Omega_{\mathrm{orb}}$.

In gamma-ray searches, in addition to the Rømer delay, we also have to correct for other effects like the Shapiro and Einstein delays. In contrast to radio observations, we do *not* have to account for the frequency-dependent dispersion caused by the Interstellar medium (ISM) because gamma rays are well above the plasma frequency of the ISM.

All of these effects are described by Lorimer & Kramer (2004) and Edwards et al. (2006). While these corrections must be included in gamma-ray searches, only the largest effects need to be included in the phase model for the derivation of a distance metric approximation.

3.1. *Parameter-space metrics*

In order to compute the metric, a simplified phase model can be used which accounts for the corrections (23) and (48):

$$\begin{aligned}\Phi(t,\boldsymbol{\lambda}) =& 2\pi f(t-t_{\mathrm{ref}}) + \pi\dot{f}(t-t_{\mathrm{ref}})^2\\ &+2\pi f r_{\mathrm{E}}\left[n_{\mathrm{x}}\cos\left(\Omega_{\mathrm{E}}t+\varphi_{\mathrm{ref}}\right)+n_{\mathrm{y}}\sin\left(\Omega_{\mathrm{E}}t+\varphi_{\mathrm{ref}}\right)\right]\\ &-2\pi f x\sin[\Omega_{\mathrm{orb}}(t-T_{\mathrm{asc}})]\,.\end{aligned} \tag{49}$$

Here the search parameters are $\boldsymbol{\lambda} = \{f,\dot{f},n_x,n_y,\Omega_{\mathrm{orb}},x,T_{\mathrm{asc}}\}$ and the terms correcting the arrival times t have been neglected for the $\dot{f}$ summand. This phase model is not sufficient for searches because it would not maintain phase coherence with a true pulsar signal. However, it is sufficient to describe how varying the signal parameters leads to loss of S/N.

The dominant components of the coherent metric for the orbital parameters are

$$\begin{aligned} g_{xx} &= 2\pi^2 f^2[1+\mathcal{O}(1/\Omega_{\mathrm{orb}}T_{\mathrm{obs}})]\,,\\ g_{\Omega_{\mathrm{orb}}\Omega_{\mathrm{orb}}} &= \frac{1}{6}\pi^2 f^2 x^2 T_{\mathrm{obs}}^2\left[1+12\frac{(t_o-T_{\mathrm{asc}})^2}{T_{\mathrm{obs}}^2}+\mathcal{O}(1/\Omega_{\mathrm{orb}}T_{\mathrm{obs}})\right]\,,\\ g_{T_{\mathrm{asc}}T_{\mathrm{asc}}} &= 2\pi^2 f^2 x^2\Omega_{\mathrm{orb}}^2[1+\mathcal{O}(1/\Omega_{\mathrm{orb}}T_{\mathrm{obs}})]\,,\\ g_{\Omega_{\mathrm{orb}}T_{\mathrm{asc}}} &= -2\pi^2 f^2 x^2\Omega_{\mathrm{orb}}T_{\mathrm{obs}}\left[\frac{(t_o-T_{\mathrm{asc}})}{T_{\mathrm{obs}}}+\mathcal{O}(1/\Omega_{\mathrm{orb}}T_{\mathrm{obs}})\right]\,,\end{aligned} \tag{50}$$

where we have assumed that the integration time span T_{obs} is much larger than the orbital period P_{orb}. Compared to the diagonal terms, as done in the text below Eq. (28), all other components are of $\mathcal{O}(1/\Omega_{\mathrm{orb}}T_{\mathrm{obs}})$.

The off-diagonal component $g_{\Omega_{\mathrm{orb}}T_{\mathrm{asc}}}$ is vanishingly small if the epoch of the ascending node is close to the middle of the gamma-ray data set, $T_{\mathrm{asc}} \approx t_0$. In principle, T_{asc} can be shifted forwards or backwards by an integer number $\mathcal{N}$ of orbital periods P_{orb} to achieve this. However, when T_{asc} is constrained, for example by optical observations, this is undesirable because it introduces uncertainties in the shifted value of T_{asc} that grow linearly with $\mathcal{N}$.

Even if $T_{\mathrm{asc}} \not\approx t_0$, our current searches ignore the off-diagonal term in the metric. The only negative consequence is that the grids are more closely spaced than needed, which reduces the efficiency of the search.

If we include the additional orbital parameters, the semi-coherent mismatch (37) can still be written in metric form

$$\bar{m}(\boldsymbol{\lambda},\boldsymbol{\lambda}_{\mathrm{psr}}) \approx n^2\bar{g}_{ab}\,\mathrm{d}\lambda^a\,\mathrm{d}\lambda^b + \mathcal{O}(\mathrm{d}\lambda^3)\,. \tag{51}$$

However, the assumptions made previously in (38) to calculate this only hold for the "isolated pulsar" parameter space coordinates $\boldsymbol{\lambda}_{\mathrm{iso}} = \{f,\dot{f},n_x,n_y\}$. They do not hold for the additional orbital parameters $\boldsymbol{\lambda}_{\mathrm{orb}} = \{\Omega_{\mathrm{orb}},x,T_{\mathrm{asc}}\}$.

If $\lambda^a \in \boldsymbol{\lambda}_{\mathrm{orb}}$ is an orbital parameter and $P_{\mathrm{orb}} \ll T_{\mathrm{coh}}$ (typical coherence time $T_{\mathrm{coh}} \approx 24\,\mathrm{d}$) the approximations

$${}_{T_{\mathrm{coh}}}\langle\partial_a\Phi\rangle(t) \approx 0\,, \tag{52a}$$

$${}_{T_{\mathrm{coh}}}\langle\partial_a\partial_b\Phi\rangle(t) \approx 0\,, \tag{52b}$$

$${}_{T_{\mathrm{obs}}}\Big\langle{}_{T_{\mathrm{coh}}}\langle\partial_a\Phi\partial_b\Phi\rangle(t')\Big\rangle(t_0) \approx {}_{T_{\mathrm{obs}}}\langle\partial_a\Phi\partial_b\Phi\rangle(t_0) \tag{52c}$$

are valid. By this, we mean that the ratio of the resulting metric to the correct metric is $1+\mathcal{O}(P_{\mathrm{orb}}/T_{\mathrm{coh}})$.

With these assumptions the semi-coherent metric $\bar{g}_{ab}$ is composed of three types of components. For the first type, the parameters $\lambda^a,\lambda^b \in \boldsymbol{\lambda}_{\mathrm{orb}}$ are orbital. For these components,

$$\bar{g}_{ab} = {}_{T_{\mathrm{obs}}}\langle\partial_a\Phi\partial_b\Phi\rangle(t_0) = g_{ab}\,, \tag{53}$$

giving the coherent result from Eq. (50).

---

[3] http://www.atnf.csiro.au/research/pulsar/psrcat

For the second type, the parameters $\lambda^a, \lambda^b \in \boldsymbol{\lambda}_{\rm iso}$ are isolated. For these components

$$\begin{aligned}\bar{g}_{ab} &= \frac{1}{2}\,{}_{T_{\rm obs}}\Big\langle {}_{T_{\rm coh}}\langle \partial_a\Phi\partial_b\Phi\rangle(t') - {}_{T_{\rm coh}}\langle \partial_a\Phi\rangle(t')\,{}_{T_{\rm coh}}\langle \partial_b\Phi\rangle(t')\Big\rangle(t_0)\\ &= \frac{1}{2}\,{}_{T_{\rm obs}}\langle \tilde{g}_{ab}(t')\rangle(t_0)\,,\end{aligned} \tag{54}$$

which is the semi-coherent result found in Eq. (42).

For the third type, one of a or b is in $\boldsymbol{\lambda}_{\rm orb}$ and the other is in $\boldsymbol{\lambda}_{\rm iso}$. One obtains the same equation as for the second type. This vanishes by virtue of Eq. (52) and because ${}_{T_{\rm coh}}\langle \partial_a\Phi\partial_b\Phi\rangle(t')$ is of order $\mathcal{O}(P_{\rm orb}/T_{\rm coh})$.

In short, the non-vanishing semi-coherent metric components reduce to earlier results. For the orbital parameters, they are the same as the coherent metric components. For the isolated (spin and celestial) parameters, they are the same as the semi-coherent metric components for an isolated pulsar. To reiterate, the non-vanishing semi-coherent orbital metric components are:

$$\begin{aligned}\bar{g}_{xx} &= 2\pi^2 f^2\,,\\ \bar{g}_{\Omega_{\rm orb}\Omega_{\rm orb}} &= \frac{1}{6}\pi^2 f^2 x^2 T_{\rm obs}^2\left(1+12\frac{(t_0-T_{\rm asc})^2}{T_{\rm obs}^2}\right),\\ \bar{g}_{T_{\rm asc}T_{\rm asc}} &= 2\pi^2 f^2 x^2 \Omega_{\rm orb}^2\,,\\ \bar{g}_{\Omega_{\rm orb}T_{\rm asc}} &= -2\pi^2 f^2 x^2 \Omega_{\rm orb}(t_0-T_{\rm asc})\,.\end{aligned} \tag{55}$$

As before, for epoch of ascending node close to the middle of the dataset, i.e. $T_{\rm asc} \approx t_0$, the semi-coherent metric is diagonal.

At the end of Section 2.5.3, we discussed the relative densities of the coherent and semi-coherent grids for isolated sources. Now we have added three additional (orbital) dimensions to the parameter space. Because the metric factors into a product of a metric on the orbital parameters and a metric on the isolated parameters, the grid may also be constructed as a product of the grids on the corresponding subspaces. For the isolated parameters, the ratio between the density of the coherent grid and the semi-coherent grid is the same as for the search for isolated pulsars. For the orbital parameters, the number of grid points needed is the same as in the coherent case. Hence, the ratio of grid densities is the same as in Eq. (43).

In Figure 1 the mismatch and its coherent-metric approximation are compared for small parameter offsets, for a realistic simulated pulsar. The corresponding plot for the semi-coherent mismatch looks very similar but has different f- and $\dot{f}$-scales. The mismatch and its metric approximation agree well for mismatch $m \leq 0.4$. This is a typical value for a search: in Appendix B, we show that maximum sensitivity for a given computing resource is obtained for an average mismatch $\hat{m} = 0.383$ (see Table 3).

The celestial parameters are not shown in Figure 1; for spider pulsars they are usually known to high precision from optical observations (e.g., from the Gaia DR2 Catalog; Gaia Collaboration et al. 2018), so no grid is required. For other pulsars where the sky position is less constrained a grid may be needed.

The search ranges for the orbital parameters are very large, and without further knowledge a full blind search is not possible. On the other hand, some searches are possible if the pulsar's companion is visible in optical/X-ray observations, which constrains the search parameters. In the next Section, we discuss a gamma-ray pulsar search design for 3FGL J1653.6–0158, which is thought to be an MSP in a circular-orbit binary (Romani et al. 2014; Saz Parkinson et al. 2016).

3.2. *Search design for circular binary*

This Section shows how to reduce the binary-pulsar search parameter space by exploiting orbital constraints from the companions.

We use the gamma-ray source 3FGL J1653.6–0158, which is predicted to be a spider pulsar (Romani et al. 2014; Kong et al. 2014), as an example. It was ranked second in Saz Parkinson et al.'s list (published 2016) of the most significant *Fermi* LAT Third Source Catalog (3FGL) unassociated sources predicted to be pulsars. The list also classifies it as a likely MSP. The gamma-ray source 3FGL J1653.6–0158 shows typical pulsar properties: a time-stable photon flux and a spectrum described by an exponential-cutoff power law.

The search ranges in spin frequency f and spin-down parameter $\dot{f}$ are guided by the known pulsar population and computational constraints. The search range is divided into YPs, with lower frequencies ($f < 44\,$Hz), and MSPs, with higher frequencies ($44\,\text{Hz} < f < 1500\,\text{Hz}$)[4]. Correspondingly, the spin-down lies between 0 and $-10^{-10}\,\text{Hz}\,\text{s}^{-1}$, for YPs, and between 0 and $-10^{-13}\,\text{Hz}\,\text{s}^{-1}$ for MSPs.

The constraints for f and $\dot{f}$ define a region in parameter space that has to be searched. The frequency dimension can be efficiently scanned using the FFT algorithm (Frigo & Johnson 2005) as described by Pletsch & Clark (2014); Clark et al. (2016) and Clark et al. (2017) for isolated pulsars. The $\dot{f}$-dimension can be covered by a uniformly spaced lattice. Special treatment for these parameters is possible: since their metric components are independent of the other parameters, so is the spacing.

In practice, the FFTs are computed in frequency intervals of bandwidth $f_{\rm BW} = 8\,$Hz. These have $f_{\rm BW}T_{\rm coh}$ frequency grid points, with frequency spacing $1/T_{\rm coh}$. In the semi-coherent stage, for two points separated by half the grid spacing, this gives a worst-case metric mismatch $m = \pi^2/24 \approx 0.411$. (As

---

[4] The high frequency-limit is around the second harmonic of the fastest known pulsar.

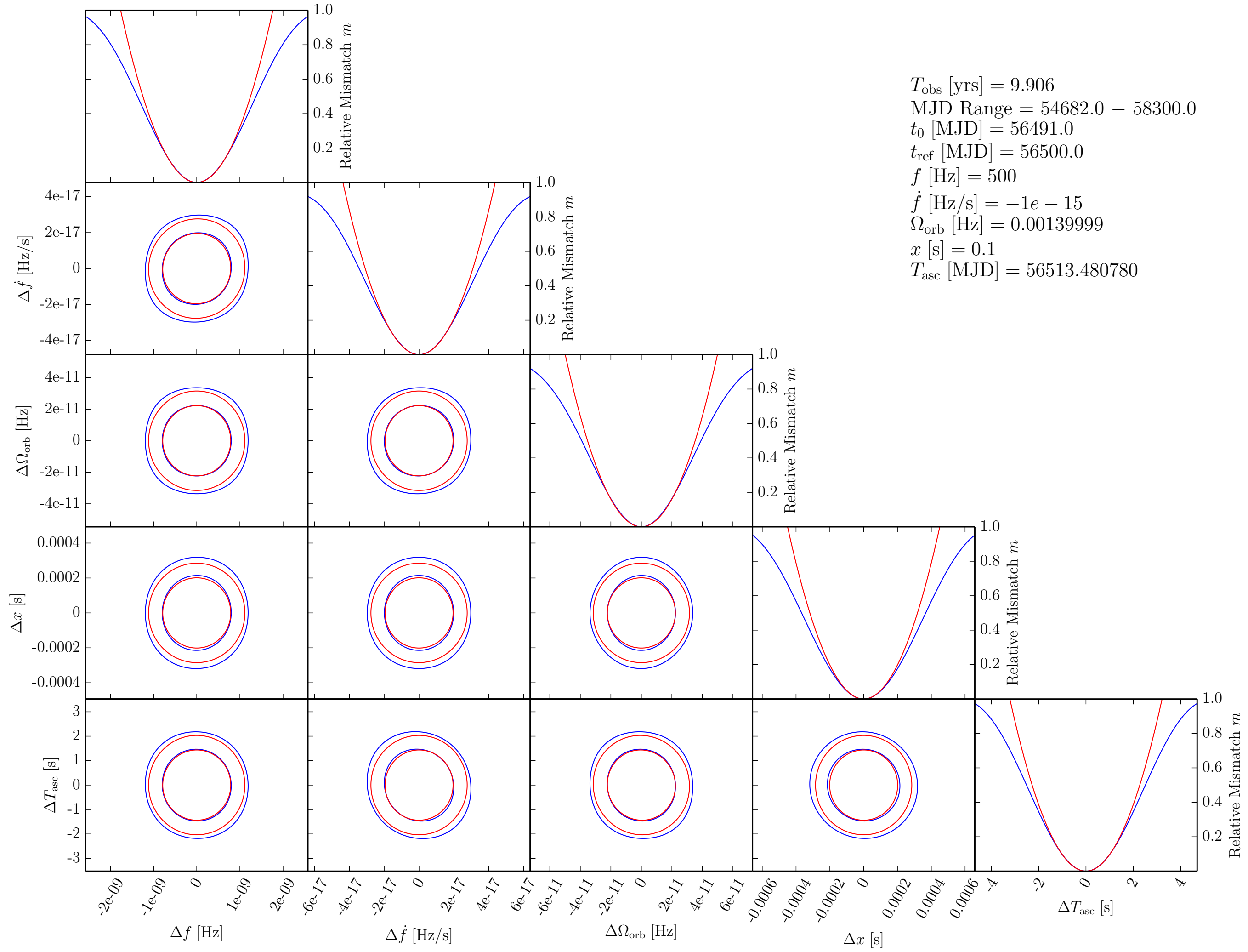

Figure 1. A comparison of the coherent metric approximation to the actual mismatch, for parameters of a simulated circular-orbit binary pulsar in 3FGL J1653.6–0158. Blue contours show the actual mismatch and red contours the metric approximation, at $m = 0.2$, and 0.4. As is generally the case (Allen 2019), the metric contours are conservative and lie inside the actual mismatch contours.

discussed in Appendix B following Eq. (B7), this can be reduced by interpolation to a worst case value of $m = 0.14$, at no significant cost.) Thus, for one $f_{\rm BW}$-interval, the computing cost is the product of the cost of a single FFT multiplied with the number of parameter-space grid points in the other dimensions.

The sky position is tightly constrained because a likely optical and X-ray counterpart with significant light-curve modulation was found (Romani et al. 2014; Kong et al. 2014; Hui et al. 2015), and proposed to be an irradiated pulsar companion. At the time, the best estimate for the position of the likely optical counterpart was from the USNO B1.0 Catalog (Monet et al. 2003). Using this instead of the 3FGL position makes it possible to search 3σ-ranges of the sky parameters with only one semi-coherent sky grid point. At high frequencies extra sky grid points are needed only in the follow-up stages. The computing costs of these are negligible compared to the semi-coherent stage. The same optical source can now be identified in the Gaia DR2 Catalog (Gaia Collaboration et al. 2018), see Table 1. For this, the uncertainty in sky position is small enough that even at $f = 1.5\,$kHz no extra sky points are needed.

The orbital parameters $\Omega_{\rm orb}$ and $T_{\rm asc}$ are directly constrained by Romani et al. (2014) using optical observations of the companion. As shown in Table 1, they found a significant modulation at a period of $P_{\rm orb} = 0.05194469 \pm 1.0 \times 10^{-7}\,$d, with epoch of ascending node $T_{\rm asc} = 56513.48078 \pm 5.2 \times 10^{-4}\,$MJD.

Additional observations allow the third orbital parameter, the projected semimajor axis of the pulsar $x = a_1 \sin i/c$ (in units of light travel time), to be constrained. Here we denote the neutron star with subscript "1" and the companion with subscript "2". Measurements of the companion's velocity amplitude $K_2 = 666.9 \pm 7.5\,{\rm km\,s^{-1}}$, together with the orbital period, imply that the pulsar mass function has the value

$$f(M_1, M_2) = \frac{P_{\rm orb} K_2^3}{2\pi G} = \frac{M_1 \sin^3 i}{(1+q)^2} = 1.60 \pm 0.05\,{\rm M}_\odot\,, \qquad (56)$$

where the mass ratio is $q = M_2/M_1$. This implies that the neutron star has mass $M_1 > 1.60 \pm 0.05\,{\rm M}_\odot$. Since redback companions have masses $M_2 \lesssim 0.4\,{\rm M}_\odot$ (Roberts 2013), this in turn implies $q < 0.25$. From Eq. (56), a mass ratio of $q = 0.25$ allows neutron-star masses up to $2.5\,{\rm M}_\odot$ for $i = 90^\circ$. (This is reassuringly conservative, since the most massive known neutron star (Cromartie et al. 2020) has mass $2.14\,{\rm M}_\odot$.) Combining the mass function with Kepler's third law $(a_1 + a_2)^3 = G(M_1 + M_2)(P_{\rm orb}/2\pi)^2$ and the center of mass definition $a_1 M_1 = a_2 M_2$ gives

$$x = \frac{q K_2 P_{\rm orb}}{2\pi c}\,. \qquad (57)$$

The upper limit for q then implies an upper limit $x \lesssim 0.2\,{\rm s}$.

It is challenging to build a search grid that covers the 3-dimensional orbital parameter space with as few points as possible. This is because (as can be seen from the metric) the orbital parameter space is not flat, so a constant-spacing lattice is not optimal. A solution to this is presented by Fehrmann & Pletsch (2014), starting with "stochastic search grids" (Babak 2008; Harry et al. 2009). A stochastic grid is built by placing grid points with a random distribution that follows the expected distribution of metric distances, while ensuring a preset minimum distance between them. The resulting grid is then optimized by nudging grid points towards regions where neighboring grid points have higher than average separation. The resulting search grid is efficient, and has a *well behaved* mismatch distribution, which simplifies the S/N distribution in the absence of signals.

The minimum number of grid points needed to cover the orbital parameter search space at mismatch m can be estimated from the proper 3-volume

$$N_{\rm orb} \approx m^{-3/2} \int \sqrt{\det g}\, {\rm d}\boldsymbol{\lambda}_{\rm orb}\,. \qquad (58)$$

Here, the integral is over the relevant range of orbital parameter space, g denotes the orbital metric from Eq. (50), and numerical factors of order unity related to the efficiency (technically "thickness"; see Appendix B) of the grid lattice have been dropped. To understand how this depends on parameters, note that the integral is proportional to

$$N_{\rm orb} \propto f^3 T_{\rm obs} \left(x_{\rm max}^3 - x_{\rm min}^3\right) \Omega_{\rm orb} \Delta\Omega_{\rm orb} \Delta T_{\rm asc}\,, \qquad (59)$$

where the search range for x is $[x_{\rm min}, x_{\rm max}]$. $\Delta\Omega_{\rm orb}$ and $\Delta T_{\rm asc}$ are the search ranges around the values of $\Omega_{\rm orb}$ and $T_{\rm asc}$ estimated from the optical modeling. Furthermore, we make the assumption that $\Delta\Omega_{\rm orb} \ll \Omega_{\rm orb}$. The strong dependency of $N_{\rm orb}$ on $x_{\rm max}$ and f means that searches for YPs (smaller f) in tight binary orbits (smaller $x_{\rm max}$) are computationally much cheaper than searches for MSPs in wide orbits. The latter are only possible if the orbital constraints are very narrow.

Table 1. Parameters and constraints for 3FGL J1653.6–0158

Parameter	Value
Range of observational data (MJD)	54682 – 58300
Reference epoch (MJD)	56500.0
Initial companion location from USNO-B1.0 catalog	
R.A., α (J2000.0)	$16^{\rm h}53^{\rm m}38\overset{\rm s}{.}07(10)$
Decl., δ (J2000.0)	$-01^\circ58'36\overset{''}{.}7(2)$
Precise companion location from Gaia catalog	
R.A., α (J2000.0)	$16^{\rm h}53^{\rm m}38\overset{\rm s}{.}05381(5)$
Decl., δ (J2000.0)	$-01^\circ58'36\overset{''}{.}8930(5)$
Constraints from probable counterpart (Romani et al. 2014)	
Ascending node epoch, $T_{\rm asc}$ (MJD)	$56513.48078 \pm 5.2 \times 10^{-4}$
Companion velocity, K_2 (km s^{-1}) . .	666.9 ± 7.5
Orbital period, $P_{\rm orb}$ (d)	$0.05194469 \pm 1.0 \times 10^{-7}$
equivalent to	
Orbital frequency, $\Omega_{\rm orb}$ (10^{-3} Hz) .	$1.3999901 \pm 2.7 \times 10^{-6}$
Derived search range	
Projected semimajor axis[a], x (s) . .	0 – 0.2

NOTE— The JPL DE405 solar system ephemeris has been used and times refer to TDB.

[a] Assuming a mass ratio of $q < 0.25$, see text following Eq. (56).

If the parameter space is small in a particular direction, this reduces the effective dimension of the parameter space and changes the formulae above. For example, denote the range of x by $[x_{\rm min}, x_{\rm max}]$. Now consider the case where $\Delta x = x_{\rm max} - x_{\rm min}$ is small enough that $g_{xx}\Delta x^2 \ll m$. Then only a single grid point is needed in the x-direction, and Eq. (58) must be replaced with a two-dimensional integral, and the exponent on m replaced with -1. Since the orbital metric components in Eq. (55) depend on the parameters, for example $g_{xx} = 2\pi^2 f^2$, this reduction in dimension can take place for certain ranges of parameters (here small frequency f) and not for others.

We can estimate the computing cost of a search for 3FGL J1653.6–0158 by computing the number of grid points

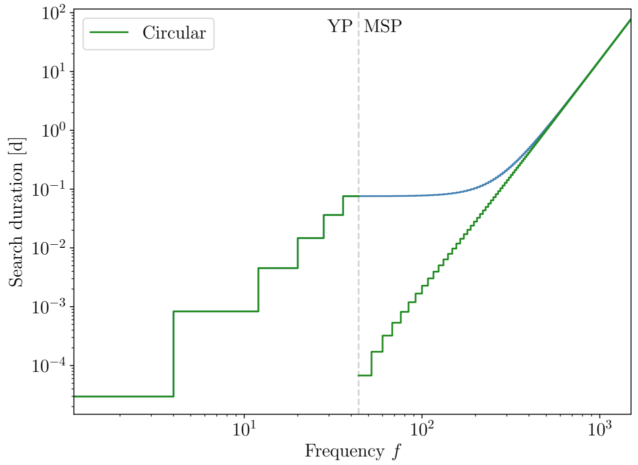

Figure 2. Predicted days on *Einstein@Home* needed to search 3FGL J1653.6–0158, assuming a circular orbit. The left green curve shows the cumulative duration of a YP search from 0 Hz up to maximum frequency f. The right green curve shows the cumulative duration of an MSP search from 44 Hz up to maximum frequency f. Their slopes are $\propto f^4$ because they are an integral over the number of orbital templates in Eq. (59). The blue curve shows the sum: the cumulative duration of a combined YP and MSP search.

in parameter space. We take $f \in [0, 44]$ Hz and $\dot{f} \in [-10^{-10}, 0]\,\mathrm{Hz\,s^{-1}}$ for the YP search, and $f \in [44, 1500]$ Hz and $\dot{f} \in [-10^{-13}, 0]\,\mathrm{Hz\,s^{-1}}$ for the MSP search from early in this Section. The remaining parameter-space search ranges are taken from Table 1 (no grid is needed over sky location). The frequency range is gridded in intervals of bandwidth $f_{\mathrm{BW}} = 8$ Hz as discussed earlier in this Section. The total computing cost is obtained by multiplying the cost of one FFT, the number of $\dot{f}$ grid points, and the number of orbital grid points (which depends on the f interval), and then summing over the f intervals. Since the orbital grid depends on frequency, a new search grid is constructed for each frequency interval, using the metric at the maximum frequency of that interval.

A convenient way to express the computing cost is in terms of search duration on *Einstein@Home*, where we assume that the project provides 25,000 GPU-hrs/week. This is shown in Figure 2 as a function of the maximum frequency searched. Searching up to $f = 1{,}500$ Hz requires less than 80 d. Note that the search cost in one frequency step is proportional to the number of orbital grid points. To search 3σ ranges in T_{asc} and Ω_{orb} within a reasonable amount of time, either the maximum f or x need to be reduced.

We can also give a general estimate for the MSP-search duration. Since the semimajor axis is typically not well constrained, we assume $x_{\min} = 0$. We evaluate Eq. (59), using Kepler's third law to replace $x_{\max}$ with the corresponding maximum searched mass ratio $q_{\max}$, obtaining

$$N_{\mathrm{orb}} \propto \frac{T_{\mathrm{obs}} G M_1}{4\pi^2 c^3} f^3 \frac{q_{\max}^3}{(1+q_{\max})^2} \left(\frac{\Delta\Omega_{\mathrm{orb}}}{\Omega_{\mathrm{orb}}}\right) \Delta T_{\mathrm{asc}}\,, \qquad (60)$$

where M_1 is the neutron star mass. As before, we assume $\dot{f} \in [-10^{-13}, 0]\,\mathrm{Hz\,s^{-1}}$ for an MSP search. The search duration up to a maximum frequency $f_{\max}$ is then

$$A \left(\frac{B(q_{\max})}{0.01}\right) \left(\frac{f_{\max}}{1\,\mathrm{kHz}}\right)^4 \left(\frac{\Delta P_{\mathrm{orb}}/P_{\mathrm{orb}}}{10^{-6}}\right) \left(\frac{\Delta T_{\mathrm{asc}}}{1\,\mathrm{min}}\right), \qquad (61)$$

where the dimensionless parenthetical factors are of order unity for typical systems of interest, and

$$B(q_{\max}) = \frac{q_{\max}^3}{(1+q_{\max})^2}\,. \qquad (62)$$

For redbacks ($q < 0.3$) one has $B(q) < 0.02$, whereas for black widows ($q < 0.08$) one has $B(q) < 4 \times 10^{-4}$. The time A depends on the details of the search and the available computing resources. A typical *Einstein@Home* search as described in this Section has $A \sim 10$ d.

In summary, this Section has shown how the circular-orbit binary pulsar search for 3FGL J1653.6–0158 can be carried out. It is computationally expensive, but by exploiting the orbital constraints it is feasible, even for high MSP frequencies. In practice, a search would start at low frequencies, gradually working up to 1.5 kHz. To further reduce cost, the search should be stopped if a pulsar is found.

While here we have considered one specific example, these methods are more broadly applicable. With them, circular orbit binary pulsar searches are practical if there are good orbital constraints from optically visible companion stars and if the pulsar's projected semimajor axis is not too large.

4. SEARCH METHOD: ECCENTRIC BINARY ORBITS

For pulsars in eccentric binary orbits, the photon arrival times have to be corrected for the line-of-sight motion $r_{z,\mathrm{ell}}(t)$, which is the projection of the eccentric orbit in the line-of-sight direction. In analogy with equation (47), we can approximate the photon emission time at the pulsar as

$$t_{\mathrm{psr}} \approx t + r_{z,\mathrm{sky}}(t) - r_{z,\mathrm{ell}}(t) \qquad (63)$$

up to $\mathcal{O}(x\Omega_{\mathrm{orb}})$. Compared with the circular case, two extra parameters are needed to describe the projected line-of-sight motion, $r_{z,\mathrm{ell}}(t)$. For now, we take these to be the orbital eccentricity e and the angle ω between the ascending node and the pericenter.

We note that the approximation to $\mathcal{O}(x\Omega_{\mathrm{orb}})$ is sufficient for the elliptical example source considered in this paper. If the value of x were larger, a higher order approximation in x would also be required (Edwards et al. 2006).

YPs with main-sequence stars as companions can have very eccentric orbits. For small orbits the pulsars tidally deform the companion, which dissipates energy. This tidally locks the companion, so that the same side of the companion faces the pulsar, and over time circularizes the orbit (Phinney 1992). This explains why old, spun-up MSPs are usually found in binaries with small or unobservable eccentricity. Only a few exceptions are known (Knispel et al. 2015).

If the energy loss in a spider system is small for each orbit, the pulsar moves around a smaller ellipse and the companion around a larger ellipse. The fixed center of mass is a focus of both ellipses, and the separation vector between pulsar and companion also traces an ellipse.

The line-of-sight variation due to the elliptical motion, $r_{z,\mathrm{ell}}(t)$, was derived by Blandford & Teukolsky (1976) and can be written as

$$r_{z,\mathrm{BT}}(t) = x\left[\sin\omega\,(\cos E - e) + \sqrt{1-e^2}\,\cos\omega\,\sin E\right]. \quad (64)$$

In this formula the label "ell" is replaced by "BT" to denote that this is the Blandford & Teukolsky model.

The eccentric anomaly E is a parameter along the pulsar path which increases with time. If ψ is the angular position of the pulsar measured from the center of the ellipse, then $\tan\psi = (1-e^2)^{1/2}\tan E$. Equivalently, project the pulsar's position parallel to the semiminor axis, onto a circle whose radius is the semimajor axis, and whose center is the center of the ellipse. Then E is the angular position of that projected point on the circle. E obeys Kepler's equation

$$M = E - e\sin E\,, \quad (65)$$

where M is the mean anomaly. This is a linear function

$$M = \Omega_{\mathrm{orb}}(t - T_0)\,, \quad (66)$$

where $T_0 = T_{\mathrm{asc}} + \omega/\Omega_{\mathrm{orb}}$ is the epoch of pericenter passage.

Unfortunately, there are some problems with the BT model and this parameterization. Kepler's equation (65) cannot be solved in closed form to find E as a function of t. Furthermore, in small-eccentricity orbits, the pericenter is not well-defined and the mismatch arising from offsets in T_0 and ω does not take the simplest possible form. For these reasons, we shift to an uncorrelated set of parameters and Taylor-expand $r_{z,\mathrm{BT}}$ as function of e.

A new set of parameters was suggested by Lange et al. (2001). These are the time of ascending node T_{asc} and two Laplace-Lagrangian parameters ϵ_1 and ϵ_2 defined via

$$T_{\mathrm{asc}} = T_0 - \omega/\Omega_{\mathrm{orb}}\,, \quad (67)$$

$$\epsilon_1 = e\sin\omega\,, \quad (68)$$

$$\epsilon_2 = e\cos\omega\,. \quad (69)$$

The parameters $\{T_0, e, \omega\}$ are given by

$$T_0 = T_{\mathrm{asc}} + \Omega_{\mathrm{orb}}^{-1}\arctan(\epsilon_1/\epsilon_2)\,, \quad (70)$$

$$e = \left(\epsilon_1^2 + \epsilon_2^2\right)^{1/2}, \quad (71)$$

$$\omega = \arctan(\epsilon_1/\epsilon_2)\,. \quad (72)$$

With the old parameters, the region of constant mismatch around a grid point is an ellipsoid whose principal directions are not parallel to the $\{T_0, e, \omega\}$ axes. In the next Section, we show that with the new parameters, the region of constant mismatch is a sphere. This simplifies the code used to optimize grid point locations.

The Rømer delay $r_{z,\mathrm{BT}}$ for the pulsar's motion can be expanded to first order in e. Following convention, we use the label "ELL1" for this linear-in-e model: $r_{z,\mathrm{BT}} = r_{z,\mathrm{ELL1}} + \mathcal{O}(e^2)$. This can be described using the parameters $\{T_0, e, \omega\}$ or the parameters $\{T_{\mathrm{asc}}, \epsilon_1, \epsilon_2\}$ as

$$r_{z,\mathrm{ELL1}}(t) = x\left[\sin(M+\omega) + \frac{e}{2}\sin(2M+\omega) - \frac{3e}{2}\sin\omega\right] \quad (73)$$

$$= x\left[\sin\phi + \frac{\epsilon_2}{2}\sin 2\phi - \frac{\epsilon_1}{2}\cos 2\phi - \frac{3}{2}\epsilon_1\right]. \quad (74)$$

We have introduced

$$\phi = \Omega_{\mathrm{orb}}(t - T_{\mathrm{asc}})\,, \quad (75)$$

which is similar to M in Eq. (66) but shifted from pericenter to ascending node. (Note that the term $-3e\sin\omega/2 = -3\epsilon_1/2$ is typically dropped, as it is time independent.)

The ELL1 approximation to the BT model can accurately track the pulsar's rotational phase for eccentricities e below some threshold value. In Appendix C, we show how this threshold depends upon the spin frequency f and semimajor axis x.

Later in the paper, in Section 4.2, we design a search for 3FGL J0523.3–2528, which is a gamma-ray source predicted to harbor a redback pulsar in an eccentric orbit. For that case, the ELL1 model is insufficient and a third-order-in-e model is needed. In Appendix C, we derive higher-order-in-e approximations to $r_{z,\mathrm{BT}}$, and demonstrate how they improve the match (decrease the mismatch) to the BT model.

4.1. *Parameter-space metrics*

In this Section, we calculate the coherent and semi-coherent parameter-space metric for the ELL1 model. Compared to the circular case, the parameter space has two extra dimensions.

Since the ELL1 model differs at first order in e from the circular model, the coherent metric also differs at first order. However, for the $\{f, \dot{f}, n_x, n_y, \Omega_{\mathrm{orb}}, x\}$ metric components, the first order terms are of $\mathcal{O}(1/\Omega_{\mathrm{orb}}T_{\mathrm{obs}})$ and can be neglected; the dominant difference is second order in e. Thus, the coherent metric components given in Eqs. (28) and (50) remain valid to first order in e.

For the ELL1 model in Eq. (73), the dominant components for the parameters $\{T_0, e, \omega\}$ are

$$\begin{aligned} g_{T_0T_0} &= 2\pi^2 f^2 x^2 \Omega_{\rm orb}^2 [1+\mathcal{O}(1/\Omega_{\rm orb}T_{\rm obs})]\,, \\ g_{ee} &= \frac{1}{2}\pi^2 f^2 x^2 [1+\mathcal{O}(1/\Omega_{\rm orb}T_{\rm obs})]\,, \\ g_{\omega\omega} &= 2\pi^2 f^2 x^2 [1+\mathcal{O}(1/\Omega_{\rm orb}T_{\rm obs})]\,, \\ g_{T_0\omega} &= -2\pi^2 f^2 x^2 \Omega_{\rm orb} [1+\mathcal{O}(1/\Omega_{\rm orb}T_{\rm obs})]\,. \end{aligned} \tag{76}$$

Note that the off-diagonal component $g_{T_0\omega}$ does not vanish. As described in the previous Section, this complicates the form of the mismatch.

We now change to the parameters $\{T_{\rm asc}, \epsilon_1, \epsilon_2\}$, for which it is convenient to use Eq. (74). For these, the diagonal components are

$$\begin{aligned} g_{T_{\rm asc}T_{\rm asc}} &= 2\pi^2 f^2 x^2 \Omega_{\rm orb}^2 [1+\mathcal{O}(1/\Omega_{\rm orb}T_{\rm obs})]\,, \\ g_{\epsilon_1\epsilon_1} &= \frac{1}{2}\pi^2 f^2 x^2 [1+\mathcal{O}(1/\Omega_{\rm orb}T_{\rm obs})]\,, \\ g_{\epsilon_2\epsilon_2} &= \frac{1}{2}\pi^2 f^2 x^2 [1+\mathcal{O}(1/\Omega_{\rm orb}T_{\rm obs})]\,. \end{aligned} \tag{77}$$

These diagonal metric components are of $\mathcal{O}(e^0)$. The terms which are linear in e are of $\mathcal{O}(1/\Omega_{\rm orb}T_{\rm obs})$, and can be neglected. Thus, the dominant diagonal e-dependent terms are of $\mathcal{O}(e^2)$. However, there are off-diagonal terms of $\mathcal{O}(e^1)$.

For small eccentricities e, the dominant metric components are given above. For completeness, we list the $\mathcal{O}(e^1)$-corrections, which are all off-diagonal:

$$\begin{aligned} g_{x\epsilon_1} &= \frac{1}{2}\pi^2 f^2 x \epsilon_1 [1+\mathcal{O}(1/\Omega_{\rm orb}T_{\rm obs})]\,, \\ g_{x\epsilon_2} &= \frac{1}{2}\pi^2 f^2 x \epsilon_2 [1+\mathcal{O}(1/\Omega_{\rm orb}T_{\rm obs})]\,, \\ g_{\Omega_{\rm orb}\epsilon_1} &= -\pi^2 f^2 x^2 \epsilon_2 T_{\rm obs} \left[\frac{(t_0-T_{\rm asc})}{T_{\rm obs}} + \mathcal{O}(1/\Omega_{\rm orb}T_{\rm obs})\right]\,, \\ g_{\Omega_{\rm orb}\epsilon_2} &= \pi^2 f^2 x^2 \epsilon_1 T_{\rm obs} \left[\frac{(t_0-T_{\rm asc})}{T_{\rm obs}} + \mathcal{O}(1/\Omega_{\rm orb}T_{\rm obs})\right]\,, \\ g_{T_{\rm asc}\epsilon_1} &= \pi^2 f^2 x^2 \Omega_{\rm orb} \epsilon_2 [1+\mathcal{O}(1/\Omega_{\rm orb}T_{\rm obs})]\,, \\ g_{T_{\rm asc}\epsilon_2} &= -\pi^2 f^2 x^2 \Omega_{\rm orb} \epsilon_1 [1+\mathcal{O}(1/\Omega_{\rm orb}T_{\rm obs})]\,. \end{aligned} \tag{78}$$

The remaining off-diagonal components of the orbital metric are of $\mathcal{O}(1/\Omega_{\rm orb}T_{\rm obs})$.

These metric components have been found to be a good approximation even for higher eccentricities where the ELL1 model is not sufficient to track the rotational phase in a search and higher order models need to be used. This might be because many of the linear-in-e terms vanish from the metric.

The semi-coherent metric components are very similar to the coherent ones. The components associated with the non-eccentric parameters $\{f, \dot{f}, n_x, n_y, \Omega_{\rm orb}, x\}$, calculated in the circular case in Eqs. (42) and (55) remain valid; they have only second-order corrections in e. For the remaining orbital parameters $\{T_{\rm asc}, \epsilon_1, \epsilon_2\}$ the semi-coherent metric components are the same as in the coherent case (this follows from Eq. (53)). Thus, the diagonal components for $\{T_{\rm asc}, \epsilon_1, \epsilon_2\}$ are

$$\begin{aligned} \bar{g}_{T_{\rm asc}T_{\rm asc}} &= 2\pi^2 f^2 x^2 \Omega_{\rm orb}^2\,, \\ \bar{g}_{\epsilon_1\epsilon_1} &= \frac{1}{2}\pi^2 f^2 x^2\,, \\ \bar{g}_{\epsilon_2\epsilon_2} &= \frac{1}{2}\pi^2 f^2 x^2\,, \end{aligned} \tag{79}$$

where we omit terms of $\mathcal{O}(1/\Omega_{\rm orb}T_{\rm obs})$. Thus, the semi-coherent metric for the ELL1 model simply adds the components above to the semi-coherent metric for the circular model.

In Figure 3, the mismatch and its coherent-metric approximation are compared for small parameter offsets, for a realistic simulated pulsar. Apart from different f- and $\dot{f}$-scales, the corresponding plot for the semi-coherent mismatch looks very similar. The mismatch agrees well with its metric approximation for mismatch $m \leq 0.5$, which is typical: in Appendix B, we show that the highest sensitivity at given computing cost for an elliptical search is obtained with an average mismatch $\hat{m} = 0.471$ (see Table 3).

The sky position parameters $\{n_x, n_y\}$ are not shown in Figure 3 because we assume that for spider pulsars they are known to high precision from optical observations.

A full blind search for binary pulsars in elliptic orbits is computationally impossible. There are too many parameter-space dimensions — even for circular orbits with reasonable parameter ranges the grid has too many points. To make a search possible, one needs tight constraints derived from optical/X-ray observations of the pulsar's companion star. In the next Section, we will discuss constraints and the search design for the probable eccentric orbit binary gamma-ray pulsar in 3FGL J0523.3–2528 (Strader et al. 2014; Saz Parkinson et al. 2016).

4.2. *Search design for low eccentricity binary*

In this Section, we discuss how to reduce the search parameter space using orbital constraints for the gamma-ray source 3FGL J0523.3–2528, presumed to be a pulsar in an eccentric binary orbit. This is similar to the circular example of Section 3.2.

The gamma-ray source itself was investigated by Saz Parkinson et al. (2016) and ranked 9th highest in a list of most significant 3FGL unassociated sources predicted to be pulsars. It shows typical pulsar-like properties: the photon flux is stable over time and the spectrum is fit by an exponential cutoff power law. The source is not in the Galactic disc, which increases the odds that it hosts an MSP.

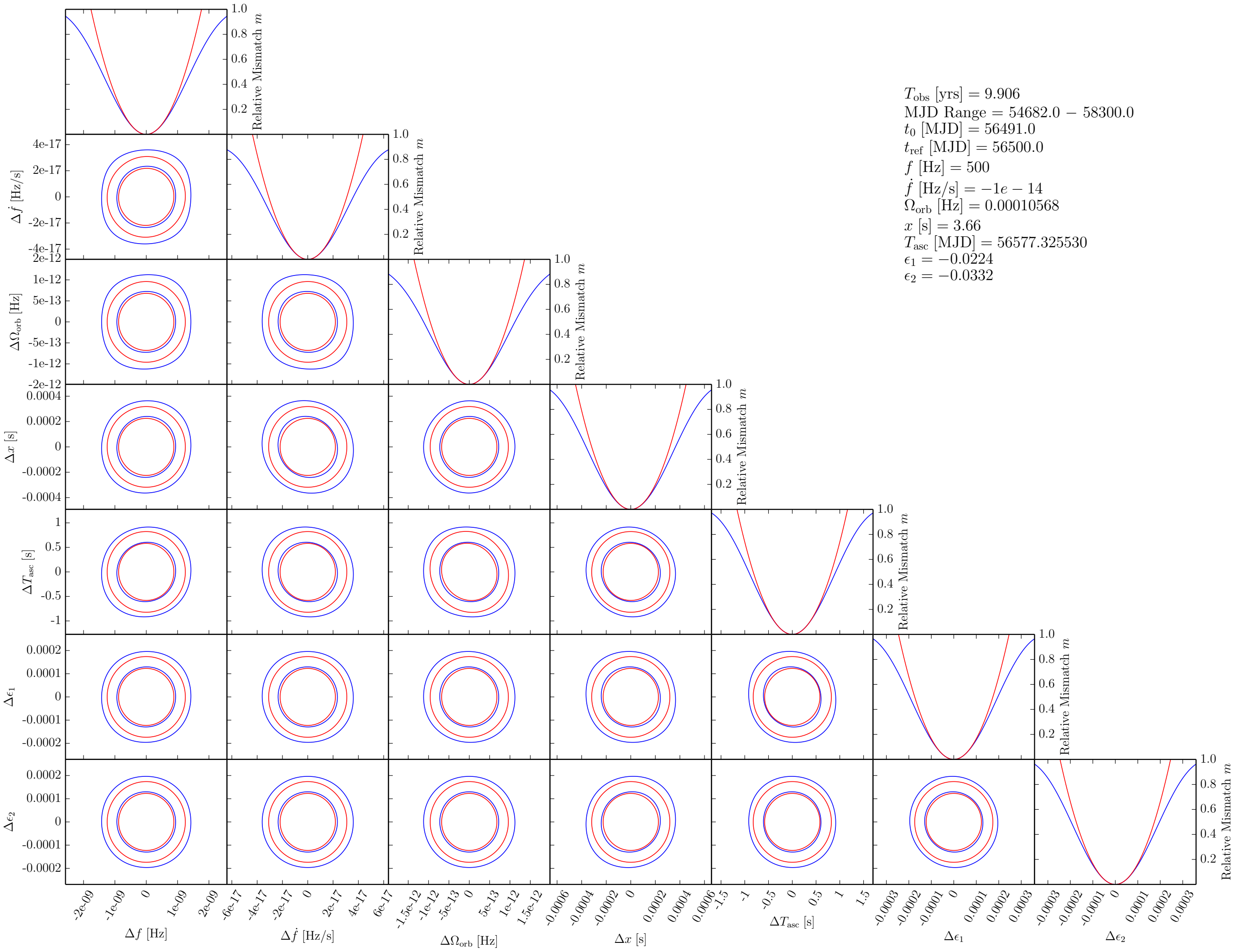

Figure 3. A comparison of the coherent metric approximation to the actual mismatch, for parameters of a simulated eccentric-orbit binary pulsar in 3FGL J0523.3–2528. Blue contours show the actual mismatch and red contours the metric approximation, at $m = 0.25$, and 0.5.

Earlier optical observations identified a likely companion and indicate an orbit with small, but not negligible, eccentricity of $e = 0.04$ (Strader et al. 2014). In contrast to the previous paragraph, this suggests that the pulsar is a YP, because binary MSPs tend to have rather circular orbits (Phinney 1992).

The frequency and spin-down search ranges are chosen following the logic of the previous search design (Section 3.2). For YPs we search $f \in [0, 44]$ Hz and $\dot{f} \in [-10^{-10}, 0]$ Hz/s. For MSPs we search $f \in [44, 1500]$ Hz and $\dot{f} \in [-10^{-13}, 0]$ Hz/s. The f-dimension is efficiently searched using FFTs with bandwidth $f_{\rm BW} = 8$ Hz and the $\dot{f}$-dimension is covered by a uniformly spaced lattice.

The sky-position search range of the probable pulsar within 3FGL J0523.3–2528 is tightly constrained from the X-ray and optical observations of the likely companion discussed above (Strader et al. 2014). At the time, the best estimate for the optical position was from the USNO-B1.0 Catalog (Monet et al. 2003). It is now also identified in the Gaia DR2 Catalog (Gaia Collaboration et al. 2018), whose pointing is so precise (see Table 2) that even at $f = 1.5$ kHz no search over sky position is required.

The orbital-parameter search ranges shown in Table 2 come from the Strader et al. (2014) analysis of the photometric and spectroscopic optical data. The orbital period and eccentricity parameters are constrained by the periodic optical-flux modulation. They assume that this arises from viewing a tidally-locked and deformed (ellipsoidal) companion at different aspect angles. Hence, the orbital period is twice the observed modulation period. (Another possible explanation for the modulation would be irradiation, but spectroscopic data does not show the orbital-phase-dependent temperature change that would be expected.) The orbital period is constrained to $P_{\rm orb} = 0.688134 \pm 0.000028$ d at epoch of superior conjunction $T_{0.5} = 56577.14636 \pm 0.0037$ MJD. The eccentric parameters $\{e, \omega\}$ fall in the ranges $e = 0.040 \pm 0.006$ and $\omega = 214 \pm 10$ deg.

The semimajor axis x is constrained using Eq. (57). This is similar to our previous example in Section 3.2, but requires fewer assumptions because the mass ratio $q = M_2/M_1$ is directly bounded from the observations. To do this, Strader et al. (2014) estimate the rotational velocity of the companion's Roche lobe from high-quality optical spectra. Combined with the companion's radial velocity $K_2 = 190.3 \pm 1.1\,\mathrm{km/s}$, this constrains the mass ratio $q = 0.61 \pm 0.06$. Returning to Eq. (57), this gives $x = 3.66 \pm 0.38$.

The parameters $\{e, \omega\}$ can be converted directly to the quantities $\{\epsilon_1, \epsilon_2\}$ needed for our search, using Eqs. (68) and (69).

For our search, we also need the epoch of ascending node T_{asc}. However, the results of Strader et al. (2014) are given in terms of the epoch of superior conjunction $T_{0.5}$. For circular orbits, $T_{0.5}$ and T_{asc} differ by $P_{\mathrm{orb}}/4$, but for eccentric orbits the relation is more complicated. To second order in e, it is

$$T_{\mathrm{asc}} = T_{0.5} + P_{\mathrm{orb}} \left(\frac{1}{4} - \frac{\epsilon_2}{\pi} - \frac{3\epsilon_1\epsilon_2}{4\pi} + \mathcal{O}(e^3) \right) . \tag{80}$$

For 3FGL J0523.3–2528 with $e = 0.04$, this $\mathcal{O}(e^2)$ approximation is more accurate than the uncertainties in the measured quantities on the rhs. (Higher-order approximations in e would be required for pulsars in binary orbits with larger eccentricities or longer orbital periods.) The resulting T_{asc} is given in Table 2.

A search for a pulsar in an eccentric orbit is very similar to one for a pulsar in a circular orbit. The only differences are that a more general model for the Rømer delay is required to track the pulsar phase, and the orbital grids need to cover five orbital dimensions. While the latter is much more complex, it can be done with the same optimized stochastic search grid construction methods that are used in the circular case.

To accurately track the rotational phase of the pulsar, requires a higher-order-in-e approximation to $r_{z,\mathrm{BT}}$ than the ELL1 model, unless the eccentricity is very small. Such approximations are computed in Appendix C. There, we also determine which order in e is sufficient.

For the case of 3FGL J0523.3–2528, a model of $\mathcal{O}(e^3)$ is sufficient. In Figure 6, we show that the rotational-phase error is negligible for the constrained parameter ranges given above.

Analogously to Eq. (58), the minimum number of grid points for the orbital parameter space can be computed from the proper 5-volume

$$N_{\mathrm{orb}} \approx m^{-5/2} \int \sqrt{\det \bar{g}}\, \mathrm{d}\boldsymbol{\lambda}_{\mathrm{orb}} . \tag{81}$$

Here, the metric has the 5 dimensions $\{x, \Omega_{\mathrm{orb}}, T_{\mathrm{asc}}, \epsilon_1, \epsilon_2\}$. This integral is proportional to

$$N_{\mathrm{orb}} \propto f^5 T_{\mathrm{obs}} \left(x_{\mathrm{max}}^5 - x_{\mathrm{min}}^5 \right) \Omega_{\mathrm{orb}} \Delta\Omega_{\mathrm{orb}} \Delta T_{\mathrm{asc}} \Delta\epsilon_1 \Delta\epsilon_2 , \tag{82}$$

where $x \in [x_{\mathrm{min}}, x_{\mathrm{max}}]$. $\Delta\Omega_{\mathrm{orb}}$, ΔT_{asc}, $\Delta\epsilon_1$, and $\Delta\epsilon_2$ are the search ranges for the corresponding parameters, and we made the assumption that $\Delta\Omega_{\mathrm{orb}} \ll \Omega_{\mathrm{orb}}$. The number of orbital grid points and subsequently the computing cost depend even stronger on f and x in an eccentric search than in a circular one.

The computing cost of a search for 3FGL J0523.3–2528 is estimated based on the number of grid points. We assume search ranges in f and $\dot{f}$ as given earlier in this Section. The remaining parameter-space ranges are given in Table 2. The required total computing cost of the search is estimated by multiplying the cost of one FFT with the number of $\dot{f}$-grid

Table 2. Parameters and constraints for 3FGL J0523.3–2528

Parameter	Value
Range of observational data (MJD)	54682 – 58300
Reference epoch (MJD)	56500.0
Initial companion location from USNO-B1.0 catalog	
R.A., α (J2000.0)	$05^{\mathrm{h}}23^{\mathrm{m}}16\overset{\mathrm{s}}{.}925(4)$
Decl., δ (J2000.0)	$-25^\circ27'36\overset{\prime\prime}{.}92(6)$
Precise companion location from Gaia catalog	
R.A., α (J2000.0)	$05^{\mathrm{h}}23^{\mathrm{m}}16\overset{\mathrm{s}}{.}931203(2)$
Decl., δ (J2000.0)	$-25^\circ27'37\overset{\prime\prime}{.}12468(4)$
Constraints from probable counterpart (Strader et al. 2014)	
Superior conjunction epoch, $T_{0.5}$ (MJD)	56577.14636 ± 0.0037
Companion velocity, K_2 (km s^{-1})	190.3 ± 1.1
Mass ratio, $q = M_2/M_1$	0.61 ± 0.06
Eccentricity, e	0.040 ± 0.006
Longitude of pericenter, ω (deg)	214 ± 10
Orbital period, P_{orb} (d)	0.688134 ± 0.000028
equivalent to	
Orbital frequency, Ω_{orb} (Hz)	$0.0001056801 \pm 4.3 \times 10^{-9}$
Derived search parameters and corresponding uncertainties	
Projected semimajor axis, x (s)	3.66 ± 0.38
Ascending node epoch, T_{asc} (MJD)	56577.32553 ± 0.00567
First Lagrange parameter, ϵ_1	-0.0224 ± 0.0091
Second Lagrange parameter, ϵ_2	-0.0332 ± 0.0089

NOTE— The JPL DE405 solar system ephemeris has been used and times refer to TDB.

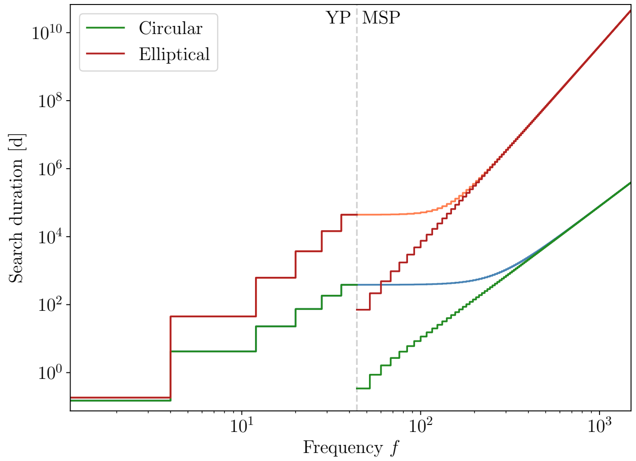

Figure 4. Predicted days on *Einstein@Home* needed to search 3FGL J0523.3–2528, assuming a circular (green/blue) or elliptical (red/orange) orbit. The left curves show the cumulative duration of a YP search from 0 Hz up to maximum frequency f. The right curves show the cumulative duration of an MSP search from 44 Hz up to maximum frequency f. Their slopes are $\propto f^4$ and $\propto f^6$; they are integrals over the number of orbital templates. The larger slope for the elliptical search arises from the two extra dimensions of search parameter space. The blue and orange curves show the sums: the cumulative duration of a combined YP and MSP search.

points, and the f-dependent number of orbital grid points, and then summing over the f intervals.

To exemplify the computing cost of a search for 3FGL J0523.3–2528, we express it in terms of search duration on *Einstein@Home*, assuming that the project provides 25,000 GPU-hours per week. This is shown in Figure 4 as a function of the maximum searched frequency. For comparison, we also show the search duration for a circular binary search, i.e. setting $e = 0$ and not searching over $\{\epsilon_1, \epsilon_2\}$. An eccentric MSP search up 1.5 kHz would take more than 100 million years on *Einstein@Home*, and even a YP search would take more than 100 years. Circular searches for YPs or MSPs up to 400 Hz would take a few 100 days. Note that the search ranges are still the 1σ ranges, so searches within the 3σ range would be more computing intensive.

In summary, this Section has shown how computing intensive a search for 3FGL J0523.3–2528 would be. An eccentric MSP search even to low frequencies ~ 100 Hz is not feasible with the current constraints, and a YP search would be very expensive. In the optical data, Strader et al. (2014) do not see evidence for a "false" eccentricity, but a circular search would be much less computing intensive than a eccentric one. With slightly tighter constraints searches up to 800 Hz could be feasible.

5. COMPARISON WITH OTHER METHODS

Similar and alternative methods are used to search for binary pulsars in data from radio telescopes and gravitational-wave detectors. In this Section, we will review these, compare them to the methods presented here, and discuss their applicability to searches for binary gamma-ray pulsars.

In addition to coming from diverse messengers and frequencies, the data have other key differences. The gamma-ray data is similar to the gravitational-wave data: the length of the data sets is months to years and the instruments simultaneously detect signals from a substantial fraction of the sky. In contrast, typical radio surveys collect data in stretches of minutes from tiny fractions of the sky. While gamma-ray data consist of discrete photon arrival times, radio and gravitational wave data are continuous. Therefore, it is not surprising that some pulsation search methods might work for one kind of data but not for the other.

For these other data sources, many methods have been employed by many individuals and groups. Here we are guided by reviews from Lorimer & Kramer (2004) for radio search methods and Messenger et al. (2015) for gravitational-wave methods. We exclude methods which require data from two detectors.

5.1. *Acceleration searches*

Time-domain "acceleration searches" have been very successful in finding new radio pulsars in binaries with orbital periods shorter than a day (see, e.g., Camilo et al. 2000). Fourier-domain acceleration searches have also been successfully used to discover binary radio pulsars (see, e.g., Ransom et al. 2001; Andersen & Ransom 2018). A similar approach to search for continuous gravitational waves is the "polynomial search" (van der Putten et al. 2010).

These searches do not use a model which describes periodic orbital motion. Instead, they assume constant acceleration along a straight line (see also Johnston & Kulkarni 1991). This accurately describes an orbiting system only if the data set is much shorter than one orbital period. Since the LAT data set is more than a decade long, acceleration searches would only find binary gamma-ray pulsars whose orbital periods were decades or longer.

It is straightforward to quantify the range of orbital periods an acceleration search is sensitive to. Assume that the data set is less than $\sim 10\%$ of the orbital period and is near the superior or inferior conjunction, where the velocity is changing linearly with time (Johnston & Kulkarni 1991). An acceleration a along the line of sight ("los") towards Earth contributes an amount

$$\dot{f}_{\mathrm{los}} = \frac{fa}{c} \tag{83}$$

to the observed spin-frequency derivative. The maximum acceleration at inferior or superior conjunction is for a circular orbit $a = cx\Omega_{\rm orb}^2$, and for an eccentric orbits $a = cx\Omega_{\rm orb}^2(1+e)/(1-e)$. Therefore, searches would be sensitive if the sum of the intrinsic pulsar spin-down and this line-of-sight contribution to the spin-down is within the search range. Since the intrinsic spin-down is usually negative, this is most likely if the acceleration towards Earth is positive, i.e. if the pulsar is near the superior conjunction.

Current blind search surveys for isolated gamma-ray pulsars are a form of acceleration search because they scan over spin-down (Clark et al. 2017). For YPs they search down to $\dot{f} = -10^{-9}$ Hz/s and for MSPs down to $\dot{f} = -10^{-13}$ Hz/s. In principle, these searches are sensitive to pulsars like the young ($f \approx 7$ Hz) binary pulsar PSR J2032+4127, which is in a $45-50$-yr orbit around its companion (Ho et al. 2017). It was found in an isolated gamma-ray search (Abdo et al. 2009c), and only afterwards it was discovered to be in a binary system (Lyne et al. 2015). The orbit is highly eccentric ($e \approx 0.93-0.99$) with $x \approx 7000-20000$ s. The maximum spin-down contribution should therefore be of order $|\max\{\dot{f}_{\rm los}\}| = 10^{-10}$ Hz/s. This is in the search range if the pulsar is near superior conjunction during the mission time.

Blind searches which assume linear acceleration, i.e. they search over constant $\dot{f}$, are only sensitive to binary pulsars with $P_{\rm orb} \gtrsim 10T_{\rm obs}$. To become sensitive to shorter orbital periods, higher-order frequency derivatives must be searched. "Jerk" searches, which include the second-order frequency derivative $\ddot{f}$, improve the sensitivity for pulsars with orbital periods in the range $P_{\rm orb} \in [7T_{\rm obs}, 20T_{\rm obs}]$ and have been successfully used in a radio pulsar search (Andersen & Ransom 2018). Alternatively, the full orbital motion may be taken into account, as in Allen et al. (2013).

5.2. *Stack/slide search*

The "stack/slide" method has been used in radio pulsar searches like the Parkes Multibeam Pulsar survey to account for binary motion (Faulkner et al. 2004). This led to the discovery of the double neutron star system PSR J1756–2251 with an orbital period of 7.7 hr (Faulkner et al. 2005). (The words "stack/slide" are used in continuous gravitational-wave searches, not to account for binary pulsar motion but rather to remove the effects of the Earth rotation and motion around the SSB (Brady & Creighton 2000; Riles 2017). That is also the case for the semi-coherent searches we describe in this paper to account for the LAT's motion around the SSB.)

In a stack/slide search the data set is broken into subsets of length $T_{\rm coh}$, corresponding to frequency bins of width $\Delta f = 1/T_{\rm coh}$. $T_{\rm coh}$ is chosen to be small enough that the Doppler modulation induced by motion of the detector around the SSB, or of the pulsar around the binary center of mass, remains within a single bin. For circular binary motion, provided that $T_{\rm coh}$ is a factor of a few smaller than $P_{\rm orb}$, this implies

$$f x \Omega_{\rm orb}^2 T_{\rm coh} < 1/T_{\rm coh}\,. \tag{84}$$

Each of these subsets is then Fourier transformed. The resulting power spectra are added (stacked) together after the Doppler modulation is compensated by shifting the frequency (slide) in each of the spectra; sources give rise to peaks in the stacked spectra. This technique is only sensitive if the subsets are much shorter than the Doppler modulation period.

This technique is useless for spider gamma-ray pulsars because detection statistics are constructed from the differences of photon arrival times. Spider pulsars have typical orbital periods of $P_{\rm orb} \lesssim 1$ d, so data subsets would have to be shorter than a few hours. Most data subsets would contain no photons. A few would contain one photon. Almost none would contain enough photons to compute the differences of photon arrival times.

Stack/slide could be used for gamma-ray pulsars in orbits where $P_{\rm orb}$ is too small for an acceleration search, but is much larger than the $T_{\rm coh} \approx 24$ d used in this paper. Using Kepler's third law, the condition of Eq. (84) can be written

$$\frac{GM_1}{c^3}\frac{q^3}{(1+q)^2} f^3 T_{\rm coh}^6 \Omega_{\rm orb}^4 < 1\,, \tag{85}$$

where M_1 is the pulsar mass and $q = M_2/M_1$ is the mass ratio. (In fact this applies provided $T_{\rm coh} \lesssim P_{\rm orb}$.) This shows that with our choice of $T_{\rm coh}$, stack/slide methods might be able to find gamma-ray pulsars with planetary companions, with orbital periods longer than ~ 1 yr and masses up to $\mathcal{O}(10)$ Earth masses.

5.3. *Power spectrum search*

The basic assumption of a "power spectrum search" is that the data set can be broken into subsets short enough that the observed spin frequency is constant in each one. This is the same assumption as in a stack/slide search. That technique is based on visual inspection and has been used to discover binary radio pulsars (see, e.g., Lyne et al. 2000).

To carry out the search, power spectra are computed for each subset. The spectra are binned in frequency and plotted with a frequency-versus-time color map. The colors show the power and make it easy to visually identify peaks in the power spectrum. A binary pulsar signal appears as a peak whose frequency varies sinusoidally with time.

The method "TwoSpect" uses a similar method to perform all-sky searches for continuous gravitational waves from sources in binary systems. The visual inspection is replaced by a second Fourier transform (hence the name TwoSpect; Goetz & Riles 2011). While no continuous gravitational waves have been detected, this technique has been used to put upper limits on continuous gravitational-wave emission from the low-mass X-ray binary Scorpius X-1 (Aasi et al. 2014).

The power spectrum search is not suitable for detecting gamma-ray spider pulsars for the same reasons as the stack/slide method.

5.4. *Sideband search*

"Sideband searches" have found many binary radio pulsars within globular clusters (Lorimer & Kramer 2004). The method has also been adapted to search for continuous gravitational waves from sources in binary systems (Messenger & Woan 2007; Sammut et al. 2014). One first carries out a search for isolated systems, as if there were no binary motion, and then looks for a characteristic structure in the results of that isolated search.

If a binary is present, orbital motion produces sidebands around a central peak at the spin frequency of the pulsar (Ransom et al. 2003). Since the isolated search does not remove the effects of the binary motion, a pulsar's power is spread over many Fourier bins (also called sidebands). This reduces the sensitivity compared to a matched-filter search.

The method is particularly useful for tight-orbit-binary pulsars where the orbital period is much smaller than the observation time span, which is the case of interest for spider pulsars. After detecting a signal, the binary parameters can be inferred from the locations and magnitudes of the sidebands and the central peak.

To see how this works, we compute the S/N of the coherent detection statistic P_n for an isolated-pulsar template, with parameters $\{\nu, \dot{f}, n_x, n_y, 0, 0, 0\}$, arising from a circular-binary pulsar with parameters $\{f, \dot{f}, n_x, n_y, x, f_{\rm orb}, T_{\rm asc}\}$, where $f_{\rm orb} = \Omega_{\rm orb}/2\pi$. This S/N is given by Eq. (17), which depends on the rotational phase difference due to the parameter mismatch:

$$\Delta\Phi(t) = 2\pi(\nu - f)(t - t_{\rm ref}) + 2\pi f x \sin[2\pi f_{\rm orb}(t - T_{\rm asc})] . \quad (86)$$

One can think of ν as denoting the pulsar frequency in the isolated search. Our derivation closely follows Ransom et al. (2003).

To compute the detection statistic P_n, we evaluate Eq. (17) with the phase mismatch (86). We first re-express $e^{in\Delta\Phi}$ using the Jacobi-Anger expansion

$$\mathrm{e}^{iz\sin\vartheta} = \sum_{m=-\infty}^{\infty} J_m(z)\mathrm{e}^{im\vartheta} , \quad (87)$$

with $z = 2\pi n f x$ and $\vartheta = 2\pi f_{\rm orb}(t - T_{\rm asc})$, where J_m is a Bessel function of the first kind. Multiplying this by $\mathrm{e}^{i2\pi n(\nu - f)(t - t_{\rm ref})}$ gives

$$\mathrm{e}^{in\Delta\Phi} = \sum_{m=-\infty}^{\infty} J_m(2\pi n f x)\mathrm{e}^{i2\pi[n(\nu-f)+m f_{\rm orb}](t-T_{\rm asc})} , \quad (88)$$

where, without loss of generality, we have set $t_{\rm ref} = T_{\rm asc}$. Since the S/N only depends on the modulus of $\mathrm{e}^{in\Delta\Phi}$, we may also set $T_{\rm asc} = 0$. We assume that there is a large number of photons from the hypothetical pulsar, which have equal weights and arrive at uniformly spaced intervals in time. The double sum $\sum_{j\neq k}$ in Eq. (17) may then be replaced by an integral over time, since

$$\begin{aligned}\sum_{j\neq k} \mathrm{e}^{in(\Delta\Phi_j - \Delta\Phi_k)} &\approx \left|\sum_j \mathrm{e}^{in\Delta\Phi_j}\right|^2 \\ &\approx \left|\frac{N}{T_{\rm obs}} \sum_{m=-\infty}^{\infty} J_m(2\pi n f x) \int_{-T_{\rm obs}/2}^{T_{\rm obs}/2} \mathrm{e}^{i2\pi[n(\nu-f)+m f_{\rm orb}]t}\,\mathrm{d}t\right|^2 .\end{aligned} \quad (89)$$

On the rhs we have included the diagonal $j = k$ term which is absent on the lhs, but is negligible in the limit where the number of photons N is large. The integral over time is

$$\frac{1}{T_{\rm obs}} \int_{-T_{\rm obs}/2}^{T_{\rm obs}/2} \mathrm{e}^{i2\pi F t}\,\mathrm{d}t = \frac{\sin(\pi F T_{\rm obs})}{\pi F T_{\rm obs}} , \quad (90)$$

with $F = n(\nu - f) + m f_{\rm orb}$. For observation times that include many orbits, the rhs of Eq. (90) is unity for $F = 0$ and is negligible otherwise. Thus, the only terms in Eq. (89) that survive are those for which $\nu = f - m f_{\rm orb}/n$. When that is satisfied, we have

$$\sum_{j\neq k} \mathrm{e}^{in\left(\Delta\Phi_j - \Delta\Phi_k\right)} \approx N^2 J_m^2(2\pi n f x) , \quad (91)$$

where m is constrained by $F = 0$. Thus, the double sum in Eq. (89) vanishes at all frequencies ν except for the "sideband frequencies" $\nu = \nu_m = f - m f_{\rm orb}/n$, where m takes on all integer values.

We now evaluate the S/N $\theta^2_{P_n}(\nu)$ from Eq. (17) by substituting in Eq. (91), assuming that the weights w_j are constant. For the reasons just given, $\theta^2_{P_n}(\nu)$ vanishes except at the discrete sideband frequencies $\nu_m = f - m f_{\rm orb}/n$. We obtain

$$\theta^2_{P_n}(\nu) = \begin{cases} J_m^2(2\pi n f x)\,\theta^2_{P_n} & \text{for } \nu = \nu_m,\ m \in \mathbb{Z} , \\ 0 & \text{otherwise} . \end{cases} \quad (92)$$

The quantity $\theta^2_{P_n}$ that appears on the rhs is given by Eq. (11). It is the S/N that the pulsar would have in an isolated search if the binary motion were absent. It is also the S/N that the pulsar would have in a binary-pulsar search at the true signal parameter values.

The structure in frequency space ν is evident from Eq.(92). As described by Ransom et al. (2003), the S/N is spread over equally-spaced sidebands around the pulsar frequency f, whose spacing is commensurate with the orbital frequency. The sideband width is $\sim 1/T_{\rm obs}$, as can be seen from Eq. (90).

In comparison with a binary pulsar search, the isolated-pulsar search has lost some S/N, since $J_m^2 \leq 1$. To recover some of the lost S/N within the isolated-pulsar search, we introduce a new test statistic that sums over the first m_{orb} sidebands around the central pulsar frequency. This cumulative sideband power may be written as

$$B_n(\nu) = \sum_{m=-m_{\text{orb}}}^{m_{\text{orb}}} P_n\left(\nu - \frac{m f_{\text{orb}}}{n}\right), \tag{93}$$

with the detection statistic $P_n(\nu)$ appropriate to an isolated-pulsar search with parameters $\{\nu, \dot{f}, n_x, n_y, 0, 0, 0\}$. (A test statistic weighing the m'th sideband in Eq. (93) by $J_m^2(2\pi n f x)$ would be more sensitive, but for simplicity it is not considered here.)

The S/N for the cumulative sideband power B_n is easily calculated. It is defined as

$$\theta_{B_n}^2 = \frac{\mathrm{E}_p[B_n] - \mathrm{E}_0[B_n]}{\sqrt{\mathrm{E}_0[B_n^2] - \mathrm{E}_0^2[B_n]}}, \tag{94}$$

where p is the pulsed fraction defined in Eq. (3). The numerator of Eq. (94) can be found from Eq. (92), which implies that $\mathrm{E}_p[P_n] - \mathrm{E}_0[P_n] = \mathrm{Var}_0[P_n]\theta_{P_n}^2 J_m^2(2\pi n f x) = 4\theta_{P_n}^2 J_m^2(2\pi n f x)$. Summing this over m gives the numerator:

$$\mathrm{E}_p[B_n] - \mathrm{E}_0[B_n] = 2\theta_{P_n}^2 \sum_{m=-m_{\text{orb}}}^{m_{\text{orb}}} J_m^2(2\pi n f x). \tag{95}$$

The denominator of Eq. (94) is defined in the absence of a signal, with $p = 0$. It is easily calculated if the noise at the different frequencies which contribute to the sum are independent. Since Poisson noise is stationary, these contributing terms will be independent if they are spaced more than one frequency bin apart, where the bins have width $1/nT_{\text{obs}}$. Since the sideband frequencies are separated by f_{orb}/n, these different terms will be independent if there are many orbits in the observation time: $f_{\text{orb}} T_{\text{obs}} \gg 1$. Each term in the denominator then has variance 4, so the sum yields $\mathrm{E}_0[B_n^2] - \mathrm{E}_0^2[B_n] = 4(2m_{\text{orb}} + 1)$. Thus, the S/N for B_n is

$$\theta_{B_n}^2 = \frac{\theta_{P_n}^2}{\sqrt{2m_{\text{orb}} + 1}} \sum_{m=-m_{\text{orb}}}^{m_{\text{orb}}} J_m^2(2\pi n f x). \tag{96}$$

To maximize this S/N, what is the optimal number of sidebands m_{orb} to include?

As shown by Ransom et al. (2003), the optimal number of sidebands to include depends upon

$$M_{\text{orb}} = [2\pi n f x], \tag{97}$$

where square brackets denotes "integer part". To see this, consider the sum which appears in Eq. (96):

$$\sum_{m=-m_{\text{orb}}}^{m_{\text{orb}}} J_m^2(2\pi n f x). \tag{98}$$

For $m_{\text{orb}} < M_{\text{orb}}$ this sum grows (approximately linearly) with increasing m_{orb}. But the addition theorem for Bessel functions ensures that Eq. (98) stops growing and approaches unity as soon as m_{orb} exceeds M_{orb}. Since the denominator of the S/N in Eq. (96) has a term that grows like $\sqrt{2m_{\text{orb}} + 1}$, the S/N is maximized for $m_{\text{orb}} = M_{\text{orb}}$. For this number of sidebands, one thus obtains

$$\theta_{B_n}^2 \approx \frac{\theta_{P_n}^2}{\sqrt{2M_{\text{orb}} + 1}} \tag{99}$$

for the expected S/N of the cumulative sideband power.

The behavior we have just described, considered alongside the definition (94) of the S/N, shows the main weakness of sideband searches. The numerator grows (approximately) linearly as we include more sidebands, meaning that we can recover all of the signal power. But, in the absence of a signal, B_n undergoes a random walk as sidebands are included, and so the denominator of Eq. (94) (the root-mean-squared of B_n in the absence of a signal) increases as $\sqrt{2M_{\text{orb}} + 1}$. Thus, in comparison with an optimal matched filter, the incoherent summation over sidebands loses a factor of $\sqrt{2M_{\text{orb}} + 1}$ in the S/N. This is explicit in Eq. (99), and makes sideband searches ineffective if there are many sidebands, as is often the case. For example, consider the potential circular-binary pulsar in 3FGL J1653.6–0158 and the potential eccentric-binary pulsar in 3FGL J0523.3–2528 discussed earlier in this paper. Their estimated parameter ranges in f and x give rise to large numbers of sidebands.

This means that sideband searches work best if only a few sidebands are expected, meaning that $2\pi x f$, the total rotational phase arising from the orbital modulation, is small. This is the case for black-widow systems, which have very light companions. The small companion mass means that the pulsar orbits very close to the center of mass, so the projected semimajor axis x is extremely small. Note that the modulation can be small even for the high frequencies f typically found for black widows.

Figure 5 illustrates this, for example, for the black-widow pulsar PSR J1311–3430, which would have been a candidate for a sideband search. The figure shows the expected optimal matched-filter S/N $\theta_{P_1}^2$ required to exceed a threshold in the expected cumulative sideband S/N $\theta_{B_1}^2 > 100$, which is a reasonable threshold for confident detection. From Eq. (99), this requires $\theta_{P_1}^2$ to exceed $100\sqrt{2M_{\text{orb}} + 1}$. Hence, M_{orb} is constant on the contour lines, which therefore denote boundaries of constant $f x$. Since the largest observed $\theta_{P_1}^2$ values for known pulsars are ~ 1000, the region below and to the left to the contour line corresponding to $\theta_{P_1}^2 = 1000$ might be considered for sideband searches.

Sideband searches within gamma-ray binaries like LS 5039 and LS I +61 303 would also be justified. These systems contain a compact object: a black hole or neutron star.

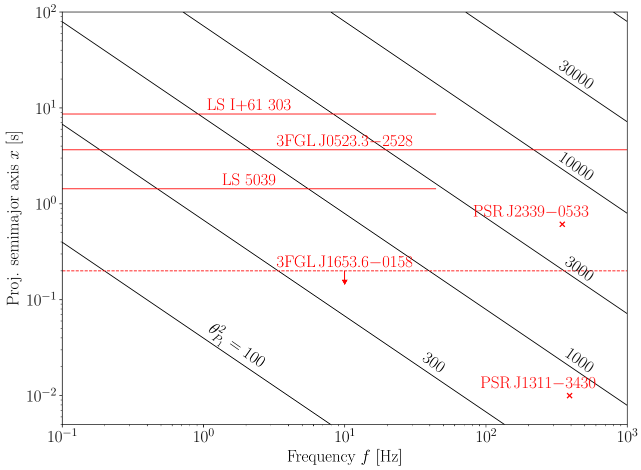

Figure 5. Comparison between the expected cumulative sideband S/N $\theta^2_{B_1}$ and the expected optimal matched-filter S/N $\theta^2_{P_1}$. For given frequency f and semimajor axis x, the black contours show the $\theta^2_{P_1}$ required to exceed a threshold $\theta^2_{B_1} > 100$. The crosses are at the locations of two known pulsars: PSR J1311–3430 and PSR J2339–0533. The red lines show four potential sideband search candidates. For the YP candidates LS 5039 and LS I+61 303, and the spider candidate 3FGL J0523.3–2528, the approximate values for the semimajor axes are known. The dashed line shows the maximum semimajor axis value for 3FGL J1653.6–0158.

Since both binaries are highly eccentric ($0.3 < e < 0.6$; Aragona et al. 2009), the compact objects could be YPs. These two candidate pulsars are both displayed in Figure 5. This is purely illustrative, since the sideband power B_n defined here is only suitable for circular-binary pulsars. Eccentric pulsars will have additional sidebands (Ransom et al. 2003), and thus must have an even higher pulsed fraction to be detectable in a sideband search.

This Section has not discussed the implementation of a practical sideband search. We would need some constraints on the parameters $f_{\rm orb}$ and x to hunt for the sidebands. If those are available from optical observations, then the sky position will be known precisely. This in turn would make a fully-coherent isolated pulsar search computationally feasible. The resulting test statistics could than be used to construct the sideband search statistic B_n of Eq. (93).

5.5. *Discussion*

The methods discussed in this Section have little applicability to searches for gamma-ray pulsars in spider systems, which are the main focus of this paper. But they are of interest for other types of binary systems.

Acceleration searches could discover binary pulsars with orbital periods comparable to, or longer than our observation time $T_{\rm obs} \sim 10\,$yr. These binaries have pulsars whose companions are very-low-mass stars or planets, in wide orbits. These pulsars might have been missed by isolated pulsar searches.

Stack/slide and power spectrum methods do not appear suitable for spider gamma-ray pulsar searches. They might potentially detect systems with orbital periods longer than our typical coherence time $T_{\rm coh} \sim 24\,$d and shorter than $T_{\rm obs} \sim 10\,$yr. However, these searches are very expensive computationally.

Sideband searches could be used to hunt for binary pulsars with low spin frequencies or in very close orbits. While these are computationally less expensive than the search methods discussed earlier in this paper, they are also considerably less sensitive.

All of these methods have a domain of applicability. Given prior knowledge and constraints on a specific target, one can investigate these different methods to determine which are feasible and to estimate which one is potentially the most sensitive.

6. CONCLUSIONS

This work presents computationally efficient methods to detect circular- and eccentric-orbit binary gamma-ray pulsars in blind searches. These generalize techniques that have been previously developed to search for isolated pulsars (Pletsch & Clark 2014).

We have presented all of the elements of this generalization. Physically, the central element is a model that accurately describes the rotational phase of a pulsar over time as would be observed at the Solar System Barycenter. In comparison with the isolated model, this must also account for the Rømer delay caused by the binary motion. A second key element are semi-coherent and coherent test statistics, along with their expected signal-to-noise ratios. The last key element are the metrics for these statistics, which measure the “distance” in parameter space between two different rotational phase models. This metric quantifies the expected fractional loss in signal-to-noise ratio, and enables the construction of efficient parameter-space grids for a search.

We have shown how these different elements can be used together to search for gamma-ray pulsars. This is analogous to the isolated pulsar case (Pletsch & Clark 2014): the most computationally efficient approach is a multistage search with several semi-coherent and coherent stages. The computing cost is proportional to the number of points in the parameter-space grid. We compute this from the metric and show how the computing cost depends on the search parameters. This in turn allows the grid spacing to be optimized, achieving the highest possible sensitivity at fixed computing cost. These methods have been very successful in discovering isolated gamma-ray pulsars (Pletsch et al. 2012b; Clark et al. 2015, 2016, 2017, 2018).

A truly blind search for binary pulsars is computationally impossible. Because the parameter space has at least 7 of the 9 possible dimensions $\{f, \dot{f}, \alpha, \delta, x, P_{\rm orb}, T_{\rm asc}, \epsilon_1, \epsilon_2\}$, too many grid points are needed to cover it. However, in some cases, the number of dimensions can be reduced and/or the corresponding search ranges can be tightly constrained by multiwavelength observations. Such searches may be characterized as "vision impaired" rather than "blind".

This paper considers two illustrative examples of this type, drawn from potential spider pulsars. Here, analysis of optical observations constrains the orbital parameters, and we show that searches of reasonable sensitivity (in some cases limited to young pulsars) are feasible. This enables "blind" searches for binary gamma-ray pulsars that were previously not feasible. This is important because these pulsars might be impossible to detect in other wavebands.

The methods of this paper, particularly the metric in parameter space, have applications beyond blind searches. There are binary pulsars which are visible in radio, optical, or X-ray, for which gamma-ray pulsations have not yet been found. For recent discoveries, precise determination of their orbital and other parameters is often not possible, since it requires observations spanning several years. The methods here are useful in such cases, to carry out efficient follow-up searches to discover gamma-ray pulsations. This way, within days or weeks after radio pulsations are discovered, the pulsar's parameters can be precisely measured over the $> 10\,$yr of elapsed LAT mission time. This approach led to the discovery of gamma-ray pulsations soon after the radio detection of the 707 Hz black-widow pulsar PSR J0952−0607 (Bassa et al. 2017; Nieder et al. 2019).

A significant shortcoming of this paper's methods is that the number of grid points, and hence the required computing resources, grow quickly with increasing frequency f and semimajor axis x. To make searches feasible, it might be necessary to balance a reduced search range (smaller maximum f and/or x) versus a reduced search sensitivity (wider grid spacing and/or shorter coherence time). Even with large computing resources like *Einstein@Home*, millisecond pulsar searches for binaries with $x \sim$ seconds are only feasible if the orbital parameters are precisely constrained.

The second significant shortcoming is that search sensitivity is lost if the pulsar's rotational phase does not match our model. This can happen for several types of pulsars and binary systems. This paper assumes that the intrinsic spin frequency f varies linearly with time. It does not include the time-dependent variations or the unpredictable frequency glitches often seen in young pulsars. This means that pulsars could be "detected" in the semi-coherent stages of a search, but are then discarded after the coherent stage, because they did not match the phase model well enough to produce a significant detection statistic (see, e.g., Clark et al. 2017). Phase model mismatch can also arise from time-dependent variations of the orbital period $P_{\rm orb}$, which seems to be common in redback systems (see, e.g., Pletsch & Clark 2015). For pulsars in short-orbital-period binaries with heavy companions, post-Keplerian gravitational corrections also have to be taken into account (see, e.g., Damour & Deruelle 1986; Edwards et al. 2006).

Because of these limitations, this paper also evaluates alternative search methods, which have previously been used in radio and gravitational-wave searches. While these may be applied to search for binary gamma-ray pulsars, only the sideband search methods appear to have some chance to detect tight-orbit spider pulsars, which are the main focus of this paper.

A more detailed study is necessary to make a fair sensitivity comparison between the sideband search and this paper's methods. Indeed, while the cumulative sideband power loses a lot of signal-to-noise ratio compared this paper's methods, it might be improved. Since the sideband structure follows a known form, one could obtain a larger S/N by assigning weights to the sidebands before summing them, rather than using equal weights as done here.

We have implemented the new methods developed in this paper in a mixture of C and Python codes. These have been tested using simulated pulsar signals, both with our own code and with the widely used TEMPO2 package (Hobbs et al. 2006). We are confident that these codes work correctly, in part because they have discovered new spider pulsars, soon to be published.

We are currently using these codes and methods to hunt for spider pulsars in the unassociated sources of the *Fermi* LAT Fourth Source Catalog Catalog. These "blind" searches are guided by orbital constraints from optical observations. The orbital grids are constructed on the computing cluster ATLAS at the Albert Einstein Institute in Hannover. The first two (semi-coherent) stages and the third (coherent) stage are all done on *Einstein@Home*, whose volunteers provide a massive computing pool. The final, less compute-demanding (H statistic) follow-up stage is done on ATLAS. To increase the computing power available in the initial stages of the search, we ported the search codes to work on *Einstein@Home*-volunteer's GPUs. The ATLAS cluster is also used to carry out follow-up gamma-ray searches of newly discovered radio pulsars, to refine the parameters as discussed above and in Nieder et al. (2019).

This paper has used the two gamma-ray sources 3FGL J1653.6−0158 and 3FGL J0523.3−2528 as examples, to show how a realistic search might be structured. Both of these searches are being carried out, and the results will be discussed in upcoming papers. A similar search for a pulsar within 3FGL J2039.6−5618 (Romani 2015; Salvetti et al. 2015) successfully detected pulsations using the methods presented here (C.J. Clark et al. 2020, in prep.).

The outlook for future searches is promising. The Gaia Catalog provides sky locations for the spider companions, which are precise enough so that no search in $\{\alpha, \delta\}$ is required. In addition, since the Large Area Telescope mission is ongoing, data sets are getting longer. Current searches use $T_{\text{obs}} \sim 11\,\text{yr}$ of data, compared with initial searches with $T_{\text{obs}} \sim 4\,\text{yr}$. Furthermore, our available computing power is also increasing with time. This means that current searches employ $T_{\text{coh}} \sim 24\,\text{d}$ in the first stage, compared with initial searches with $T_{\text{coh}} \sim 12\,\text{d}$. Since search sensitivity scales with $(T_{\text{coh}} T_{\text{obs}})^{1/4}$ (Pletsch & Clark 2014), our current sensitivity has increased by more than 50%. We believe that $\mathcal{O}(10-30)$ of the unassociated sources in the 4FGL Catalog are undiscovered spider pulsars, and that we can find some of them.

There are systems which are very likely to be spider gamma-ray pulsars, for which the orbital constraints are not yet good enough to perform searches. These include the five redback pulsar candidates: 3FGL J0212.1+5320 (Li et al. 2016; Linares et al. 2017), 3FGL J0744.1–2523 (Salvetti et al. 2017), 3FGL J0838.8–2829 (Halpern et al. 2017), 3FGL J0954.8–3948 (Li et al. 2018), and the recent 4FGL J2333.1–5527 (Swihart et al. 2020). We hope that this work helps motivate additional optical observations to improve these constraints, and enable new gamma-ray pulsar discoveries.

ACKNOWLEDGMENTS

We thank Anne Archibald and Andrea Belfiore for encouraging us to look into sideband-search methods. This work was supported by the Max-Planck-Gesellschaft (MPG), by the Deutsche Forschungsgemeinschaft (DFG) through an Emmy Noether Research Grant, No. PL 710/1-1 (PI: Holger J. Pletsch) and by National Science Foundation grants 1104902 and 1816904. This work was supported by an STSM Grant from COST Action CA16214. C.J.C. acknowledges support from the ERC under the European Union's Horizon 2020 research and innovation programme (grant agreement No. 715051; Spiders).

Software: TEMPO2 (Hobbs et al. 2006; Edwards et al. 2006), `matplotlib` (Hunter 2007), `NumPy` (Oliphant 2006; van der Walt et al. 2011)

APPENDIX

A. EXPECTATION VALUES OF SIGNAL STATISTICS

Here we show how to calculate the expectation values of signal statistics. The statistics depend upon the $j = 1, \ldots, N$ modeled pulsar rotation phases at the photon arrival times t_j. To simplify the language and notation, we suppose that the vector of parameters $\boldsymbol{\lambda} = \{f, \dot{f}, \alpha, \delta\}$ is fixed, and denote the modeled rotation phases by $\Phi_j = \Phi(t_j, \boldsymbol{\lambda}) = \Phi(t_{\text{psr}}(t_j, \alpha, \delta), f, \dot{f})$. Sums and products over j, k, ℓ run from $1, \ldots, N$ unless otherwise specified. Finally, we write "the phase of the j'th photon", rather than "the modeled pulsar rotational phase associated with the j'th photon".

Our key assumption is that the phase of each photon is an independent (hence uncorrelated) random variable. This is justified because the number of photons detected is much less than one per pulsar revolution. The phase Φ_j of the j'th photon is drawn from the distribution $F_j(\Phi_j)$ as given in Eq. (3). Thus, using Eq. (4), the probability distribution function of Φ_j is

$$F_j(\Phi_j) = \frac{1}{2\pi} + \frac{p w_j}{2\pi} \sum_{n=-\infty}^{\infty} \gamma_n \mathrm{e}^{in\Phi_j}\,, \tag{A1}$$

where the Fourier coefficients γ_n are defined by Eq. (5) for $n > 0$, by $\gamma_n = \gamma_{-n}^*$ for $n < 0$, and by $\gamma_0 = 0$ for $n = 0$.

The expectation value of any quantity $Q(\Phi_1, \ldots, \Phi_N)$ is now given by

$$E[Q] = \int_0^{2\pi} \mathrm{d}\Phi_1 F_1(\Phi_1) \cdots \int_0^{2\pi} \mathrm{d}\Phi_N F_N(\Phi_N) Q(\Phi_1, \cdots, \Phi_N)\,, \tag{A2}$$

where the statistical independence of the rotation phases allows the probability density to be written as a product. For example the expected value of $\exp(-in\Phi_j)$ is

$$\begin{aligned} E[\mathrm{e}^{-in\Phi_j}] &= \int_0^{2\pi} \mathrm{d}\Phi_j F_j(\Phi_j) \mathrm{e}^{-in\Phi_j} \\ &= \delta_{n0} + \frac{p w_j}{2\pi} \sum_{m=-\infty}^{\infty} \int_0^{2\pi} \mathrm{d}\Phi \gamma_m \mathrm{e}^{i(m-n)\Phi} \\ &= \delta_{n0} + p\, w_j\, \gamma_n\,, \end{aligned} \tag{A3}$$

where δ_{nm} is the Kronecker delta, giving unity for $n = 0$.

The expected value of the coherent power signal statistic Eq. (6) is

$$E[P_n] = \kappa^{-2} \sum_{j,k} w_j w_k \prod_{\ell} \int_0^{2\pi} \mathrm{d}\Phi_\ell F_\ell(\Phi_\ell) \mathrm{e}^{in(\Phi_k - \Phi_j)}\,. \tag{A4}$$

In the product above, only two terms are nontrivial, for which either $\ell = k$ or $\ell = j$. The integrand does not depend upon the other $N-2$ integration variables, whose corresponding integrals give unity, since the probability density is normalized.

One obtains

$$\begin{aligned} E[P_n] &= \kappa^{-2}\sum_j w_j^2 + \kappa^{-2}p^2\sum_{\substack{j,k\\ j\neq k}} w_j^2 w_k^2 |\gamma_n|^2 \\ &= 2+2p^2|\gamma_n|^2\left[\sum_j w_j^2 - \frac{\sum_j w_j^4}{\sum_j w_j^2}\right]. \end{aligned} \tag{A5}$$

On the first line, the first sum comes from terms with $j = k$ and the second sum from terms where $j \neq k$, and we have used Eq. A3 to simplify both terms.

B. MAXIMAL SENSITIVITY AT FIXED COMPUTING COST

The sensitivity of a search can be quantified via the pulse fraction p defined in Eq. (3). More sensitive searches can detect sources with smaller values of p.

If infinite computing power were available, we would employ the fully coherent detection statistics H or P_1, and the sensitivity of a search would only be limited by the data. To determine that ultimate sensitivity, consider the expected S/N $\theta^2_{P_1}$ given in Eq. (11). A point in parameter space where $\theta^2_{P_1}$ exceeded some threshold $\theta^2_{\rm threshold}$ (established by the desired false alarm and false dismissal probabilities) would be counted as a detection. A reasonable detection threshold might be $\theta^2_{\rm threshold} = 50$, corresponding to pulse fraction sensitivity $p^2 > \theta^2_{\rm threshold}/|\gamma_1|^2\mu T_{\rm obs}$. For typical values of $\mu T_{\rm obs} = 500$ effective photons and $|\gamma_1|^2 = 0.8$, this gives an ultimate, data-limited sensitivity of $p^2 > 0.13$.

In practice, with limited computing power, we adopt the multi-stage hierarchical approach described in Section 2.3. A sensible choice is to use most of the computing power in the first, semi-coherent stage. Roughly speaking, this is because a signal will only be found if it rises above the detection threshold in the first stage of the search[5]. Hence we will assume that our sensitivity is limited by the first semi-coherent search stage.

The maximum possible sensitivity of the semi-coherent stage is determined by the threshold on the semi-coherent S/N, whose expected value is given in Eq. (36). The threshold is lower than before, typically $\theta^2_{S_1} > \theta^2_{\rm threshold} = 10$. Using search parameters from Eq. (27) and later in that Section gives a minimum detectable pulse fraction of $p^2 > \theta^2_{\rm threshold}/|\gamma_1|^2\mu\sqrt{T_{\rm obs}T_{\rm coh}} = 0.31$. As before, this is the theoretical sensitivity that could be achieved with unlimited computing power, but employing the semi-coherent statistic.

In practice, we must take the computing cost into account. This cost is proportional to the number of grid points in parameter space at which the detection statistic is calculated. Reducing the number of grid points (corresponding to a larger average mismatch) loses some S/N but the additional computing power may be used to increase the coherence time $T_{\rm coh}$, which increases the S/N. What compromise maximizes the search sensitivity for a given computing cost?

To find the optimal balance between the worst-case grid mismatch m and the coherent integration time $T_{\rm coh}$, we maximize the sensitivity with the constraint that the compute power is fixed, as described in Prix & Shaltev (2012) and Pletsch & Clark (2014). What is important is the rate at which the number of grid points grows with increasing $T_{\rm coh}$, which in turn depends upon the dimension of the parameter space.

The number of dimensions d in the search parameter space is determined by our prior knowledge. To quantify that, we use $n_{\rm orb}$ (possible values 3 or 5) for the number of orbital parameters searched, and $n_{\rm sky}$ (possible values 0 or 2) for the number of sky dimensions searched, so $d = 2 + n_{\rm orb} + n_{\rm sky}$. In the case of an eccentric binary with poorly known position, we have the full parameter space discussed in the main text, $\{f, \dot{f}, n_x, n_y, \Omega_{\rm orb}, x, T_{\rm asc}, \epsilon_1, \epsilon_2\}$, so $n_{\rm orb} = 5$, $n_{\rm sky} = 2$, and $d = 9$. For an eccentric binary whose position is precisely known (for example from optical observations), $\{n_x, n_y\}$ are omitted from the search, $n_{\rm orb} = 5$, $n_{\rm sky} = 0$, and $d = 7$. For a circular binary whose position is precisely known, $\{\epsilon_1, \epsilon_2\}$ are also omitted, so $n_{\rm orb} = 3$, $n_{\rm sky} = 0$, and $d = 5$.

The smallest detectable pulse fraction (averaged over signal location in parameter space) may be written as

$$p^2_{S_1} = \frac{\theta^2_{\rm threshold}}{(1-\hat{m})|\gamma_1|^2\mu\sqrt{T_{\rm obs}T_{\rm coh}}}\,. \tag{B6}$$

Here, $\hat{m}$ represents the average (over parameter space) mismatch of the grid (Prix & Shaltev 2012).

The construction of our parameter space grid is described following Eq. (55); its average mismatch may be estimated as follows. Within a given 8 Hz frequency interval, the grid is the direct product of an equally-spaced grid in the frequency direction, an equally-spaced grid in the $\dot{f}$ direction, a 2-dimensional hexagonal lattice in sky position $\{n_x, n_y\}$, and an optimized stochastic grid in the orbital parameters. Below, we call these "subgrids". To determine the computing cost, we need to count the number of grid points in these subgrids, and multiply them together.

Because the metric has no off-diagonal terms that couple the different subgrids, the average parameter space mismatch $\hat{m}$ can be written as

$$\hat{m} = \hat{m}_f + \hat{m}_{\dot{f}} + \hat{m}_{\rm sky} + \hat{m}_{\rm orb}\,, \tag{B7}$$

where $\hat{m}_f$ is the average mismatch in the frequency dimension (if all other parameters are exactly matched to the signal), and $\hat{m}_{\dot{f}}$, $\hat{m}_{\rm sky}$, $\hat{m}_{\rm orb}$ are the corresponding average mismatches in the $\dot f$, sky, and orbital subgrids (if all other parameters are exactly matched to the signal).

---

[5] Of course this depends upon the choice of threshold and the region of parameter space around a candidate which is searched in the subsequent stages. If the full parameter space is searched for each candidate, then the statement is false!

The frequency dimension is searched with an FFT whose frequency spacing $\mathrm{d}f = 1/T_{\rm coh}$. For the worst case, which is two points separated by $\mathrm{d}f/2$, the quadratic metric approximation predicts a mismatch $\bar g_{ff}/(2T_{\rm coh})^2 = \pi^2/24 = 0.411$, and hence an average mismatch $\hat m_f = 0.14$. As is often the case, the quadratic approximation slightly overestimates the mismatch; the Spherical Ansatz of Allen (2019) predicts a worst-case $m = \sin^2(\sqrt{\pi^2/24}) \approx 0.36$ which agrees well with the numerically measured value given in Section 5.2 of Pletsch & Clark (2014). In fact, as described before Eq. (42) of that paper, we can reduce the average mismatch to $\hat m_f = 0.075$ at almost no extra computational cost, by interpolating the frequency spectrum.

The $\dot f$ subgrid has uniform spacing $d\dot f$, and is an example of a regular lattice. For regular lattices, the average mismatch $\hat m$ is related to the worst-case mismatch m via $\hat m = \xi m$, where $\xi \in [0,1]$ is a lattice-dependent dimensionless geometrical factor called “thickness’ (Prix & Shaltev 2012). Here we have a (one-dimensional) hypercubic grid, for which $\xi = 1/3$, so the average mismatch $\hat m_{\dot f} = m_{\dot f}/3$, where $m_{\dot f} = \bar g_{\dot f \dot f}(d\dot f/2)^2 = \pi^2 T_{\rm coh}^2 T_{\rm obs}^2 d\dot f^2/288$ is the maximal mismatch in the $\dot f$ dimension. (Since the differences are small, for simplicity we do not employ the Spherical Ansatz further.)

The sky subgrid is a hexagonal lattice with thickness $\xi = 5/12 \approx 0.416$. Hence, $\hat m_{\rm sky} = 0.416 m_{\rm sky}$, where $m_{\rm sky}$ is the worst-case sky mismatch.

The orbital parameter grid has an average mismatch which is well-estimated during the process of its construction, and can be easily controlled via the parameter that determines when new points are added to the stochastic bank.

The computing cost is the product of the number of grid points in the non-frequency dimensions with the cost of a single FFT. The number of grid points can be estimated using arguments like those given in deriving Eq. (58). In each of the different subgrids, the number of grid points is proportional to $\hat m^{-D/2}$ where $\hat m$ is the average mismatch in that subgrid, and D is the dimension of that subgrid. Hence the number of grid points in the $\dot f$ subgrid is proportional to $T_{\rm coh}\hat m_{\dot f}^{-1/2}$ and the number of grid points in the sky subgrid is proportional to $T_{\rm coh}^{n_{\rm sky}}\hat m_{\rm sky}^{-n_{\rm sky}/2}$. The number of grid points in the orbital subgrid is proportional to $\hat m_{\rm orb}^{-n_{\rm orb}/2}$ and is independent of $T_{\rm coh}$. Since the cost of an FFT is proportional to $T_{\rm coh}\log T_{\rm coh}$, this gives a total computing cost C

$$C = C_0\,\hat m_{\dot f}^{-1/2}\,\hat m_{\rm sky}^{-n_{\rm sky}/2}\,\hat m_{\rm orb}^{-n_{\rm orb}/2}\,T_{\rm coh}^{2+n_{\rm sky}}\,. \tag{B8}$$

Here C_0 is a constant, and following Pletsch & Clark (2014), we have omitted the slowly-varying logarithmic factor from the cost of the FFT.

The method of Lagrange multipliers can be used to maximize sensitivity $p_{S_1}^{-2}$ at fixed computing cost[6]. The quantity we extremize is

$$\begin{aligned}\mathcal{L} &= p_{S_1}^{-2} + \lambda C \\ &= c_1(1-\hat m)T_{\rm coh}^{1/2} + \lambda c_2 \hat m_{\dot f}^{-1/2}\hat m_{\rm sky}^{-n_{\rm sky}/2}\hat m_{\rm orb}^{-n_{\rm orb}/2}T_{\rm coh}^{s}\,,\end{aligned} \tag{B9}$$

where λ is the Lagrange multiplier, $s = 2 + n_{\rm sky}$, and c_1 and c_2 are constants (independent of the average mismatches and $T_{\rm coh}$). Extremizing $\mathcal{L}$ with respect to the coherence time and the three different average mismatches gives

$$\begin{aligned}\frac{\partial\mathcal{L}}{\partial T_{\rm coh}} &= \frac{c_1}{2}(1-\hat m)T_{\rm coh}^{-1/2} + s\lambda c_2\hat m_{\dot f}^{-1/2}\hat m_{\rm sky}^{-n_{\rm sky}/2}\hat m_{\rm orb}^{-n_{\rm orb}/2}T_{\rm coh}^{s-1} = 0\\ \frac{\partial\mathcal{L}}{\partial \hat m_{\dot f}} &= -c_1 T_{\rm coh}^{1/2} - \tfrac{1}{2}\lambda c_2\hat m_{\dot f}^{-3/2}\hat m_{\rm sky}^{-n_{\rm sky}/2}\hat m_{\rm orb}^{-n_{\rm orb}/2}T_{\rm coh}^{s} = 0\\ \frac{\partial\mathcal{L}}{\partial \hat m_{\rm sky}} &= -c_1 T_{\rm coh}^{1/2} - \tfrac{n_{\rm sky}}{2}\lambda c_2\hat m_{\dot f}^{-1/2}\hat m_{\rm sky}^{-n_{\rm sky}/2-1}\hat m_{\rm orb}^{-n_{\rm orb}/2}T_{\rm coh}^{s} = 0\\ \frac{\partial\mathcal{L}}{\partial \hat m_{\rm orb}} &= -c_1 T_{\rm coh}^{1/2} - \tfrac{n_{\rm orb}}{2}\lambda c_2\hat m_{\dot f}^{-1/2}\hat m_{\rm sky}^{-n_{\rm sky}/2}\hat m_{\rm orb}^{-n_{\rm orb}/2-1}T_{\rm coh}^{s} = 0\,,\end{aligned}$$

where we have made use of Eq. (B7) to evaluate the derivatives of $\hat m$.

To find the average mismatches that maximize the sensitivity at fixed computing cost, combine the first equation in turn with the second or third or fourth: $T_{\rm coh}$ drops out and one obtains a closed form for the corresponding average mismatch. The independence from coherence time $T_{\rm coh}$ in the binary pulsar case was previously shown for the isolated pulsar case by Pletsch & Clark (2014). For example, to solve for $\hat m_{\dot f}$, multiply the first equation by $T_{\rm coh}^{1/2}$, multiply the second equation by $2s\hat m_{\dot f}T_{\rm coh}^{-1/2}$, and add them. One obtains $(1-\hat m)/2 - 2s\hat m_{\dot f} = 0$, whose solution is $\hat m_{\dot f} = (1-\hat m)/4s$. Doing this for all three combinations yields

$$\begin{aligned}\hat m_{\dot f} &= \frac{1-\hat m}{4(2+n_{\rm sky})}\,,\\ \hat m_{\rm orb} &= \frac{1-\hat m}{4(2+n_{\rm sky})}n_{\rm orb}\,, \text{ and}\\ \hat m_{\rm sky} &= \frac{1-\hat m}{4(2+n_{\rm sky})}n_{\rm sky}\,.\end{aligned} \tag{B10}$$

Note that the optimal solution has equal average “per-dimension” mismatch in the non-frequency subgrids. From Eq. (B7) it follows that $\hat m - \hat m_f$ is the sum of the three terms above, and since $d-1 = 1 + n_{\rm orb} + n_{\rm sky}$, we have $\hat m - \hat m_f = (1-\hat m)(d-1)/4(2+n_{\rm sky})$. The solution is

$$\hat m = \frac{1 + n_{\rm orb} + n_{\rm sky} + 4(2+n_{\rm sky})\hat m_f}{9 + n_{\rm orb} + 5n_{\rm sky}}\,. \tag{B11}$$

---

[6] One obtains the same result by maximizing any negative power of p_{S_1}.

Table 3. A comparison of computationally unlimited and optimal computationally-limited semi-coherent searches, showing mismatches and sensitivity. The columns show the average template bank mismatch $\hat{m}$, and the average mismatches in the $\dot{f}$, sky and orbital subgrids. (Note that the average per-dimension mismatch is constant.) Then the corresponding maximum $\dot{f}$ and sky mismatch are listed with the (square of the) minimum detectable pulsed fraction p. The first row shows the ideal semi-coherent case where the grid points are infinitesimally spaced and the compute cost is infinite. The next three rows illustrate smaller and smaller binary-system parameter spaces. The final row is for an isolated pulsar with unknown sky position.

Search	$\hat{m}$	$\hat{m}_{\dot{f}}$	$\hat{m}_{\rm sky}$	$\hat{m}_{\rm orb}$	$m_{\dot{f}}$	m_{sky}	$p^2_{S_1}$
Infinite computing cost (zero mismatch) grid	0	0	0	0	0	0	0.307
All parameters unknown ($n_{\rm sky} = 2$, $n_{\rm orb} = 5$)	0.383	0.039	0.077	0.193	0.116	0.093	0.497
Elliptical, known position ($n_{\rm sky} = 0$, $n_{\rm orb} = 5$)	0.471	0.066	0	0.330	0.198	0.159	0.580
Circular, known position ($n_{\rm sky} = 0$, $n_{\rm orb} = 3$)	0.383	0.077	0	0.231	0.231	0.185	0.497
Isolated ($n_{\rm sky} = 2$, $n_{\rm orb} = 0$)	0.221	0.049	0.097	0	0.146	0.117	0.394

Thus we have

$$\begin{aligned}\hat{m}_{\dot{f}} &= \frac{1-\hat{m}_f}{9+n_{\rm orb}+5n_{\rm sky}}\,,\\ \hat{m}_{\rm orb} &= \frac{1-\hat{m}_f}{9+n_{\rm orb}+5n_{\rm sky}}n_{\rm orb}\,,\ \text{and}\\ \hat{m}_{\rm sky} &= \frac{1-\hat{m}_f}{9+n_{\rm orb}+5n_{\rm sky}}n_{\rm sky}\,,\end{aligned} \tag{B12}$$

which in turn allows us to determine the average and maximum mismatch in each of the subgrids, and the corresponding search sensitivity compared with an extremely finely spaced (but computationally very expensive) semi-coherent search.

In practice, after setting the mismatch as given by this optimal point, one adjusts the coherence time $T_{\rm coh}$ to be as long as allowed by the available computing resources. What does this imply about the sensitivity? Above, we showed that with reasonable assumptions, a semi-coherent search can detect a pulsed fraction $p^2 > 0.31$ if there are infinite computing resources. With finite computing resources, this is increased by a factor of $1/(1-\hat{m}) = (9+n_{\rm orb}+5n_{\rm sky})/4(2+n_{\rm sky})(1-\hat{m}_f)$, as can be seen from Eq. (B6). The corresponding loss of sensitivity is shown in Table 3. The achievable pulsed-fraction sensitivity is not far from the ideal case.

This analysis extends previous work (Pletsch & Clark 2014), which assumed a grid with fixed thickness $\xi = 1/3$ in all dimensions. However, this is not the case for current searches. Here, we have considered a grid which is a product of subgrids, each of which can have different geometrical properties, as used in existing searches. If we assume fixed thickness, then our results and in particular the final line of Table 3 agree with Eq. (H2) from Pletsch & Clark (2014).

C. HIGH ORDER PHASE MODEL FOR ELLIPTICAL BINARIES

The main text uses a linear-in-e "ELL1" approximation to the correct "BT" line-of-sight motion in eccentric orbits. Here, we consider higher orders in the eccentricity e. The BT model is given in Eq. (64):

$$r_{z,\rm BT}(t) = x\left[\sin\omega(\cos E - e) + \cos\omega\sqrt{1-e^2}\sin E\right]\,, \tag{C13}$$

$$E - e\sin E = M\,, \tag{C14}$$

$$M = \Omega_{\rm orb}(t-T_0)\,. \tag{C15}$$

We express this as

$$r_{z,\rm BT}(t) = x\left[\sin\omega\sum_{n=0}^{\infty}\alpha_n(e)\cos(nM) + \cos\omega\sum_{n=1}^{\infty}\beta_n(e)\sin(nM)\right]\,, \tag{C16}$$

where $\alpha_n(e)$ and $\beta_n(e)$ are power series in e. The goal here is to find these functions, and to determine the appropriate order needed for our searches. (Taff (1985) gives an expansion of $\sin E$ and $\cos E$ in powers of e, but does not give a similar expansion for the line-of-sight motion.)

For the derivation of the power series we introduce the Bessel functions and some of their properties. For positive integers n the Bessel function can be expressed as the power series

$$J_n(x) = \sum_{m=0}^{\infty}\frac{(-1)^m\left(\frac{x}{2}\right)^{2m+n}}{m!(n+m)!} \tag{C17}$$

or in integral form as

$$J_n(x) = \frac{1}{2\pi}\int_0^{2\pi}\cos(n\theta - x\sin\theta)\,{\rm d}\theta\,. \tag{C18}$$

The relation

$$J_{n-1}(x) + J_{n+1}(x) = \frac{2n}{x}J_n(x) \tag{C19}$$

is also needed.

Following Taff (1985), we start with the Fourier expansion of $\cos E$:

$$\cos E = \frac{\hat{\alpha}_0}{2} + \sum_{n=1}^{\infty}\hat{\alpha}_n\cos(nM)\,. \tag{C20}$$

It has Fourier coefficients

$$\hat{\alpha}_n = \frac{1}{\pi}\int_0^{2\pi} \cos E \cos(nM)\, \mathrm{d}M\,. \tag{C21}$$

Using Kepler's equation (C14) to write M and dM as functions of E, along with the integral form above, one obtains

$$\hat{\alpha}_n = \frac{2}{n}\frac{\mathrm{d}J_n(n\,e)}{\mathrm{d}(n\,e)}\,. \tag{C22}$$

Using the power series above, this may be written as

$$\hat{\alpha}_n(e) = \begin{cases} \sum\limits_{m=0}^{\infty} \frac{(-1)^m\,(2m+n)}{n\,m!\,(m+n)!} \left(\frac{n}{2}\right)^{2m+n-1} e^{2m+n-1} & ,\ n \geq 1 \\ -\frac{1}{2}e & ,\ n = 0\,. \end{cases} \tag{C23}$$

The analogous calculation for $\sin E$ gives

$$\sin E = \sum_{n=1}^{\infty} \hat{\beta}_n \sin(nM) \tag{C24}$$

with coefficients

$$\hat{\beta}_n = \frac{1}{\pi}\int_0^{2\pi} \sin E \sin(nM)\, \mathrm{d}M\,, \tag{C25}$$

where

$$\begin{aligned} \hat{\beta}_n =& \frac{2}{ne}J_n(n\,e) \\ =& \sum_{m=0}^{\infty} \frac{(-1)^m \left(\frac{n\,e}{2}\right)^{2m+n-1}}{m!\,(n+m)!} e^{2m+n-1} \end{aligned} \tag{C26}$$

is obtained using the recursion relation above.

To obtain β from $\sqrt{1-e^2}\hat{\beta}$, we first express

$$\sqrt{1-e^2} = \sum_{k=0}^{\infty} e^{2k} \left(\sum_{l=0}^{2k} (-1)^l \binom{1/2}{l}\binom{1/2}{2k-l} \right)\,, \tag{C27}$$

where we have introduced the generalized binomial coefficient

$$\binom{r}{k} = \frac{r\cdot(r-1)\cdots(r-(k-1))}{k!}\,. \tag{C28}$$

The Cauchy product of $\sqrt{1-e^2}$ and $\hat{\beta}$ gives

$$\begin{aligned} \beta_n(e) = \sum_{m=0}^{\infty} e^{2m+n-1} \sum_{k=0}^{m} \frac{\left(\frac{n}{2}\right)^{(2m-2k+n-1)}}{(m-k)!(n+m-k)!} \\ \times \sum_{l=0}^{2k} (-1)^{m-k+l} \binom{1/2}{l}\binom{1/2}{2k-l}\,. \end{aligned} \tag{C29}$$

The α_n follow directly from $\hat{\alpha}_n$, and differ only for $n = 0$.

We list the results to 11th order. (A similar calculation (Dhurandhar & Vecchio 2001) gives the coefficients to seventh order, but without a general formula.) The α's are given by:

$$\alpha_0 = -\frac{3}{2}e\,, \tag{C30a}$$

$$\begin{aligned} \alpha_1 =& 1 - \frac{3}{8}e^2 + \frac{5}{192}e^4 - \frac{7}{9216}e^6 + \frac{1}{81920}e^8 \\ & - \frac{11}{88473600}e^{10}\,, \end{aligned} \tag{C30b}$$

$$\alpha_2 = \frac{1}{2}e - \frac{1}{3}e^3 + \frac{1}{16}e^5 - \frac{1}{180}e^7 + \frac{1}{3456}e^9\,, \tag{C30c}$$

$$\begin{aligned} \alpha_3 =& \frac{3}{8}e^2 - \frac{45}{128}e^4 + \frac{576}{5120}e^6 - \frac{729}{40960}e^8 \\ & + \frac{8019}{4587520}e^{10}\,, \end{aligned} \tag{C30d}$$

$$\alpha_4 = \frac{1}{3}e^3 - \frac{2}{5}e^5 + \frac{8}{45}e^7 - \frac{8}{189}e^9\,, \tag{C30e}$$

$$\alpha_5 = \frac{125}{384}e^4 - \frac{4375}{9216}e^6 + \frac{15625}{57344}e^8 - \frac{4296875}{49545216}e^{10}\,, \tag{C30f}$$

$$\alpha_6 = \frac{27}{80}e^5 - \frac{81}{140}e^7 + \frac{729}{1792}e^9\,, \tag{C30g}$$

$$\alpha_7 = \frac{16807}{46080}e^6 - \frac{117649}{163840}e^8 + \frac{63412811}{106168320}e^{10}\,, \tag{C30h}$$

$$\alpha_8 = \frac{128}{315}e^7 - \frac{512}{567}e^9\,, \tag{C30i}$$

$$\alpha_9 = \frac{531441}{1146880}e^8 - \frac{52612659}{45875200}e^{10}\,, \tag{C30j}$$

$$\alpha_{10} = \frac{78125}{145152}e^9\,, \tag{C30k}$$

$$\alpha_{11} = \frac{2357947691}{3715891200}e^{10}\,. \tag{C30l}$$

The β's are given by:

$$\begin{aligned} \beta_1 =& 1 - \frac{5}{8}e^2 - \frac{11}{192}e^4 - \frac{457}{9216}e^6 - \frac{23479}{737280}e^8 \\ & - \frac{2014861}{88473600}e^{10}\,, \end{aligned} \tag{C31a}$$

$$\beta_2 = \frac{1}{2}e - \frac{5}{12}e^3 + \frac{1}{24}e^5 - \frac{1}{45}e^7 - \frac{379}{34560}e^9\,, \tag{C31b}$$

$$\begin{aligned} \beta_3 =& \frac{3}{8}e^2 - \frac{51}{128}e^4 + \frac{543}{5120}e^6 - \frac{219}{8192}e^8 \\ & - \frac{18141}{4587520}e^{10}\,, \end{aligned} \tag{C31c}$$

$$\beta_4 = \frac{1}{3}e^3 - \frac{13}{30}e^5 + \frac{13}{72}e^7 - \frac{739}{15120}e^9\,, \tag{C31d}$$

$$\beta_5 = \frac{125}{384}e^4 - \frac{4625}{9216}e^6 + \frac{144625}{516096}e^8 - \frac{4611125}{49545216}e^{10}\,, \tag{C31e}$$

$$\beta_6 = \frac{27}{80}e^5 - \frac{135}{224}e^7 + \frac{3753}{8960}e^9\,, \tag{C31f}$$

$$\beta_7 = \frac{16807}{46080}e^6 - \frac{218491}{294912}e^8 + \frac{65160739}{106168320}e^{10}\,, \tag{C31g}$$

$$\beta_8 = \frac{128}{315}e^7 - \frac{2624}{2835}e^9\,, \tag{C31h}$$

$$\beta_9 = \frac{531441}{1146880}e^8 - \frac{53675541}{45875200}e^{10}\,, \tag{C31i}$$

$$\beta_{10} = \frac{78125}{145152}e^9\,, \tag{C31j}$$

$$\beta_{11} = \frac{2357947691}{3715891200}e^{10}\,. \tag{C31k}$$

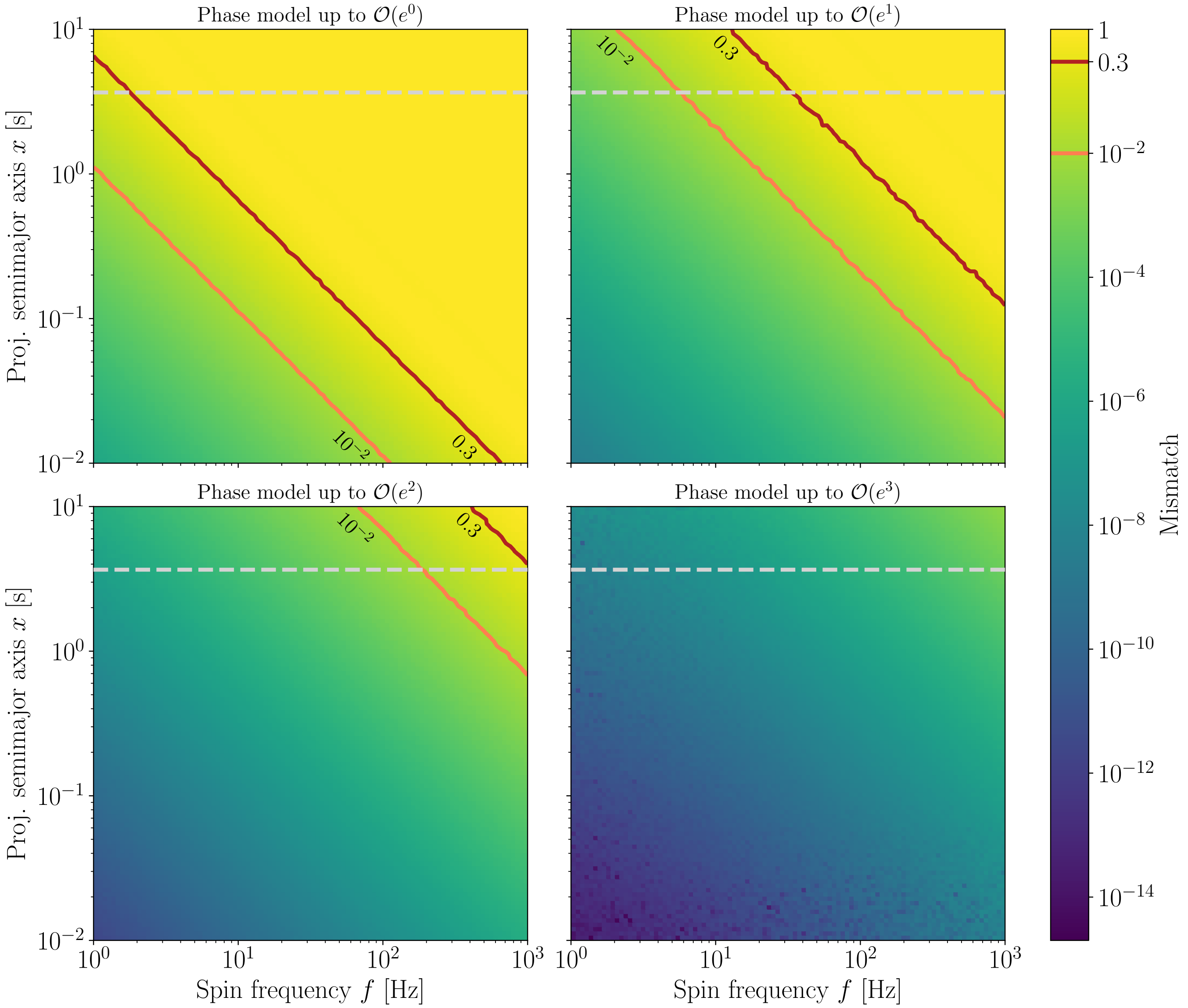

Figure 6. Mismatch between the BT model and models truncated at orders e^0, e^1, e^2, and e^3, for the source 3FGL J0523.3–2528 with $e = 0.04$. This is computed on a grid of 100×100 simulated pulsar signals, with equally spaced $\log_{10} f/\mathrm{Hz} \in [0,3]$, and $\log_{10} x/\mathrm{s} \in [-2,1]$. The gray, dashed line indicates the semimajor axis $x = 3.66$ of the likely pulsar in 3FGL J0523.3–2528. The slopes of the constant-mismatch contours are the same for different models because e is fixed.

A line-of-sight model accurate to $\mathcal{O}(e^k)$ requires retaining terms up to and including α_{k+1} and β_{k+1}. Depending on the search parameters $\{f, x, e\}$ different orders of these Taylor series will be required.

Consider the source 3FGL J0523.3–2528. The expected eccentricity is $e \sim 0.04$. To find the appropriate order in e, we simulated 10,000 realizations of a pulsar in 3FGL J0523.3–2528, with different spin frequencies f and semimajor axes x. Figure 6 shows the mismatches which arise from using approximations of different orders in e, compared to the full BT model. For high frequencies the mismatch m is significant $m \sim 0.3$ (S/N loss of up to 30%) for the $\mathcal{O}(e^2)$-model. A sensible choice is the $\mathcal{O}(e^3)$-model, for which the mismatch is below 1% for frequencies $f < 1\,\mathrm{kHz}$.

For systems with different eccentricities, we can also provide guidance. Since most of the known spider pulsars are MSPs, we simulated 10,000 realizations of a 1 kHz-pulsar with different semimajor axes x and eccentricities e. Figure 7 shows the mismatches that arise up to sixth orders in e.

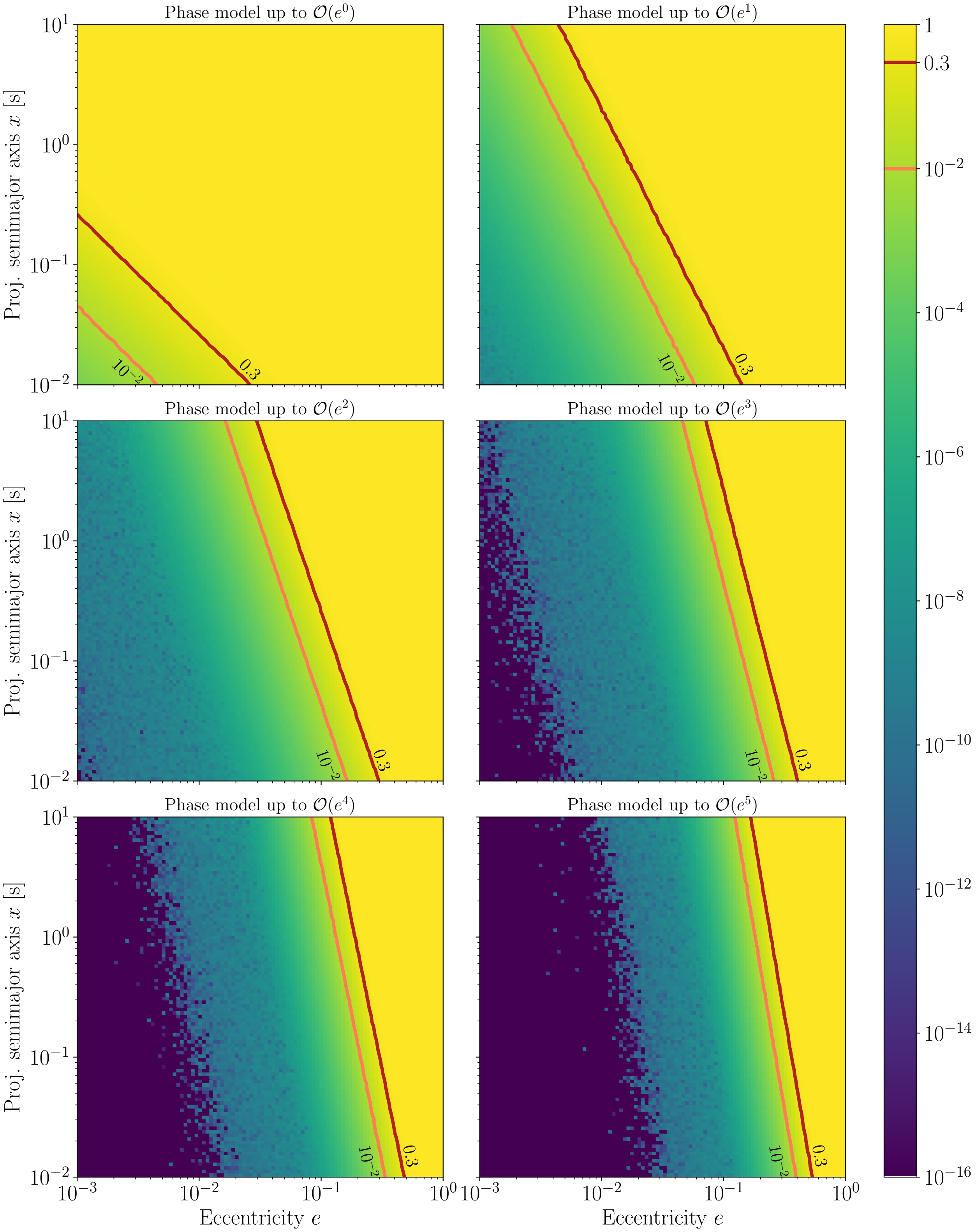

Figure 7. Same as Figure 6, but varying the eccentricity e with fixed frequency $f = 1\,\mathrm{kHz}$, and going up to e^5. The mismatch is computed on a grid of 100×100 simulated pulsar signals, with equally spaced $\log_{10} e \in [-3, 0]$, and $\log_{10} x/\mathrm{s} \in [-2, 1]$.

REFERENCES

Aasi, J., Abbott, B. P., Abbott, R., et al. 2014, PhRvD, 90, 062010, doi: 10.1103/PhysRevD.90.062010

Abdo, A. A., Ackermann, M., Atwood, W. B., et al. 2009a, ApJL, 695, L72, doi: 10.1088/0004-637X/695/1/L72

—. 2009b, ApJ, 699, 1171, doi: 10.1088/0004-637X/699/2/1171

Abdo, A. A., Ackermann, M., Ajello, M., et al. 2009c, Science, 325, 840, doi: 10.1126/science.1175558

Abdollahi, S., Acero, F., Ackermann, M., et al. 2020, ApJS, 247, 33, doi: 10.3847/1538-4365/ab6bcb

Allen, B. 2019, PhRvD, 100, 124004, doi: 10.1103/PhysRevD.100.124004

Allen, B., Knispel, B., Cordes, J. M., et al. 2013, ApJ, 773, 91, doi: 10.1088/0004-637X/773/2/91

Andersen, B. C., & Ransom, S. M. 2018, ApJL, 863, L13, doi: 10.3847/2041-8213/aad59f

Aragona, C., McSwain, M. V., Grundstrom, E. D., et al. 2009, ApJ, 698, 514, doi: 10.1088/0004-637X/698/1/514

Atwood, W. B., Abdo, A. A., Ackermann, M., et al. 2009, ApJ, 697, 1071, doi: 10.1088/0004-637X/697/2/1071

Babak, S. 2008, Classical and Quantum Gravity, 25, 195011, doi: 10.1088/0264-9381/25/19/195011

Balasubramanian, R., Sathyaprakash, B. S., & Dhurandhar, S. V. 1996, PhRvD, 53, 3033, doi: 10.1103/PhysRevD.53.3033

Bassa, C. G., Pleunis, Z., Hessels, J. W. T., et al. 2017, ApJL, 846, L20, doi: 10.3847/2041-8213/aa8400

Bickel, P., Kleijn, B., & Rice, J. 2008, ApJ, 685, 384, doi: 10.1086/590399

Blandford, R., & Teukolsky, S. A. 1976, ApJ, 205, 580, doi: 10.1086/154315

Brady, P. R., & Creighton, T. 2000, PhRvD, 61, 082001, doi: 10.1103/PhysRevD.61.082001

Camilo, F., Lorimer, D. R., Freire, P., Lyne, A. G., & Manchester, R. N. 2000, ApJ, 535, 975, doi: 10.1086/308859

Caraveo, P. A. 2014, ARA&A, 52, 211, doi: 10.1146/annurev-astro-081913-035948

Clark, C. J., Pletsch, H. J., Wu, J., et al. 2015, ApJL, 809, L2, doi: 10.1088/2041-8205/809/1/L2

—. 2016, ApJL, 832, L15, doi: 10.3847/2041-8205/832/1/L15

Clark, C. J., Wu, J., Pletsch, H. J., et al. 2017, ApJ, 834, 106, doi: 10.3847/1538-4357/834/2/106

Clark, C. J., Pletsch, H. J., Wu, J., et al. 2018, Science Advances, 4, eaao7228, doi: 10.1126/sciadv.aao7228

Cromartie, H. T., Fonseca, E., Ransom, S. M., et al. 2020, Nature Astronomy, 4, 72, doi: 10.1038/s41550-019-0880-2

Damour, T., & Deruelle, N. 1986, Ann. Inst. Henri Poincaré Phys. Théor, 44, 263

de Jager, O. C., Raubenheimer, B. C., & Swanepoel, J. W. H. 1989, A&A, 221, 180

Dhurandhar, S. V., & Vecchio, A. 2001, PhRvD, 63, 122001, doi: 10.1103/PhysRevD.63.122001

Edwards, R. T., Hobbs, G. B., & Manchester, R. N. 2006, MNRAS, 372, 1549, doi: 10.1111/j.1365-2966.2006.10870.x

Faulkner, A. J., Stairs, I. H., Kramer, M., et al. 2004, MNRAS, 355, 147, doi: 10.1111/j.1365-2966.2004.08310.x

Faulkner, A. J., Kramer, M., Lyne, A. G., et al. 2005, ApJL, 618, L119, doi: 10.1086/427776

Fehrmann, H., & Pletsch, H. J. 2014, PhRvD, 90, 124049, doi: 10.1103/PhysRevD.90.124049

Frigo, M., & Johnson, S. G. 2005, Proceedings of the IEEE, 93, 216, doi: 10.1109/JPROC.2004.840301

Fruchter, A. S., Stinebring, D. R., & Taylor, J. H. 1988, Nature, 333, 237, doi: 10.1038/333237a0

Gaia Collaboration, Brown, A. G. A., Vallenari, A., et al. 2018, A&A, 616, A1, doi: 10.1051/0004-6361/201833051

Goetz, E., & Riles, K. 2011, Classical and Quantum Gravity, 28, 215006, doi: 10.1088/0264-9381/28/21/215006

Guillemot, L., Johnson, T. J., Venter, C., et al. 2012, ApJ, 744, 33, doi: 10.1088/0004-637X/744/1/33

Halpern, J. P., Strader, J., & Li, M. 2017, ApJ, 844, 150, doi: 10.3847/1538-4357/aa7cff

Harry, I. W., Allen, B., & Sathyaprakash, B. S. 2009, PhRvD, 80, 104014, doi: 10.1103/PhysRevD.80.104014

Ho, W. C. G., Ng, C.-Y., Lyne, A. G., et al. 2017, MNRAS, 464, 1211, doi: 10.1093/mnras/stw2420

Hobbs, G. B., Edwards, R. T., & Manchester, R. N. 2006, MNRAS, 369, 655, doi: 10.1111/j.1365-2966.2006.10302.x

Hui, C. Y., Park, S. M., Hu, C. P., et al. 2015, ApJ, 809, 68, doi: 10.1088/0004-637X/809/1/68

Hunter, J. D. 2007, Computing in Science and Engineering, 9, 90, doi: 10.1109/MCSE.2007.55

Johnston, H. M., & Kulkarni, S. R. 1991, ApJ, 368, 504, doi: 10.1086/169715

Kerr, M. 2011, ApJ, 732, 38, doi: 10.1088/0004-637X/732/1/38

Knispel, B., Lyne, A. G., Stappers, B. W., et al. 2015, ApJ, 806, 140, doi: 10.1088/0004-637X/806/1/140

Kong, A. K. H., Jin, R., Yen, T.-C., et al. 2014, ApJL, 794, L22, doi: 10.1088/2041-8205/794/2/L22

Lange, C., Camilo, F., Wex, N., et al. 2001, MNRAS, 326, 274, doi: 10.1046/j.1365-8711.2001.04606.x

Li, K.-L., Kong, A. K. H., Hou, X., et al. 2016, ApJ, 833, 143, doi: 10.3847/1538-4357/833/2/143

Li, K.-L., Hou, X., Strader, J., et al. 2018, ApJ, 863, 194, doi: 10.3847/1538-4357/aad243

Linares, M., Miles-Páez, P., Rodríguez-Gil, P., et al. 2017, MNRAS, 465, 4602, doi: 10.1093/mnras/stw3057

Lorimer, D. R., & Kramer, M. 2004, Handbook of Pulsar Astronomy

Lyne, A. G., Mankelow, S. H., Bell, J. F., & Manchester, R. N. 2000, MNRAS, 316, 491, doi: 10.1046/j.1365-8711.2000.03517.x

Lyne, A. G., Stappers, B. W., Keith, M. J., et al. 2015, MNRAS, 451, 581, doi: 10.1093/mnras/stv236

Manchester, R. N., Hobbs, G. B., Teoh, A., & Hobbs, M. 2005, AJ, 129, 1993, doi: 10.1086/428488

Meinshausen, N., Bickel, P., & Rice, J. 2009, Ann. Appl. Stat., 3, 38, doi: 10.1214/08-AOAS180

Messenger, C., & Woan, G. 2007, Classical and Quantum Gravity, 24, S469, doi: 10.1088/0264-9381/24/19/S10

Messenger, C., Bulten, H. J., Crowder, S. G., et al. 2015, PhRvD, 92, 023006, doi: 10.1103/PhysRevD.92.023006

Monet, D. G., Levine, S. E., Canzian, B., et al. 2003, AJ, 125, 984, doi: 10.1086/345888

Nieder, L., Clark, C. J., Bassa, C. G., et al. 2019, ApJ, 883, 42, doi: 10.3847/1538-4357/ab357e

Oliphant, T. E. 2006, A guide to NumPy, Vol. 1 (Trelgol Publishing USA)

Owen, B. J. 1996, PhRvD, 53, 6749, doi: 10.1103/PhysRevD.53.6749

Phinney, E. S. 1992, Philosophical Transactions of the Royal Society of London Series A, 341, 39, doi: 10.1098/rsta.1992.0084

Pletsch, H. J., & Clark, C. J. 2014, ApJ, 795, 75, doi: 10.1088/0004-637X/795/1/75

—. 2015, ApJ, 807, 18, doi: 10.1088/0004-637X/807/1/18

Pletsch, H. J., Guillemot, L., Fehrmann, H., et al. 2012a, Science, 338, 1314, doi: 10.1126/science.1229054

Pletsch, H. J., Guillemot, L., Allen, B., et al. 2012b, ApJ, 744, 105, doi: 10.1088/0004-637X/744/2/105

Prix, R., & Shaltev, M. 2012, PhRvD, 85, 084010, doi: 10.1103/PhysRevD.85.084010

Ransom, S. M., Cordes, J. M., & Eikenberry, S. S. 2003, ApJ, 589, 911, doi: 10.1086/374806

Ransom, S. M., Greenhill, L. J., Herrnstein, J. R., et al. 2001, ApJL, 546, L25, doi: 10.1086/318062

Riles, K. 2017, Modern Physics Letters A, 32, 1730035, doi: 10.1142/S021773231730035X

Roberts, M. S. E. 2013, in IAU Symposium, Vol. 291, Neutron Stars and Pulsars: Challenges and Opportunities after 80 years, ed. J. van Leeuwen, 127–132, doi: 10.1017/S174392131202337X

Romani, R. W. 2015, ApJL, 812, L24, doi: 10.1088/2041-8205/812/2/L24

Romani, R. W., Filippenko, A. V., & Cenko, S. B. 2014, ApJL, 793, L20, doi: 10.1088/2041-8205/793/1/L20

Salvetti, D., Mignani, R. P., De Luca, A., et al. 2015, ApJ, 814, 88, doi: 10.1088/0004-637X/814/2/88

—. 2017, MNRAS, 470, 466, doi: 10.1093/mnras/stx1247

Sammut, L., Messenger, C., Melatos, A., & Owen, B. J. 2014, PhRvD, 89, 043001, doi: 10.1103/PhysRevD.89.043001

Saz Parkinson, P. M., Xu, H., Yu, P. L. H., et al. 2016, ApJ, 820, 8, doi: 10.3847/0004-637X/820/1/8

Saz Parkinson, P. M., Dormody, M., Ziegler, M., et al. 2010, ApJ, 725, 571, doi: 10.1088/0004-637X/725/1/571

Smith, D. A., Guillemot, L., Kerr, M., Ng, C., & Barr, E. 2017, ArXiv e-prints. https://arxiv.org/abs/1706.03592

Strader, J., Chomiuk, L., Sonbas, E., et al. 2014, ApJL, 788, L27, doi: 10.1088/2041-8205/788/2/L27

Swihart, S. J., Strader, J., Urquhart, R., et al. 2020, ApJ, 892, 21, doi: 10.3847/1538-4357/ab77ba

Taff, L. G. 1985, Celestial mechanics: A computational guide for the practitioner

van der Putten, S., Bulten, H. J., van den Brand, J. F. J., & Holtrop, M. 2010, in Journal of Physics Conference Series, Vol. 228, Journal of Physics Conference Series, 012005, doi: 10.1088/1742-6596/228/1/012005

van der Walt, S., Colbert, S. C., & Varoquaux, G. 2011, Computing in Science and Engineering, 13, 22, doi: 10.1109/MCSE.2011.37